Space Sci Rev (2020) 216:110
https://doi.org/10.1007/s11214-020-00732-4

# Studying the Composition and Mineralogy of the Hermean Surface with the Mercury Radiometer and Thermal Infrared Spectrometer (MERTIS) for the BepiColombo Mission: An Update

**H. Hiesinger[1] · J. Helbert[1] · G. Alemanno[1] · K.E. Bauch[1] · M. D'Amore[1] · A. Maturilli[1] · A. Morlok[1] · M.P. Reitze[1] · C. Stangarone[1] · A.N. Stojic[1] · I. Varatharajan[1] · I. Weber[1] · the MERTIS Co-I Team[1]**

Received: 15 March 2020 / Accepted: 1 September 2020 / Published online: 11 September 2020
© The Author(s) 2020

**Abstract** Launched onboard the BepiColombo Mercury Planetary Orbiter (MPO) in October 2018, the Mercury Radiometer and Thermal Infrared Spectrometer (MERTIS) is on its way to planet Mercury. MERTIS consists of a push-broom IR-spectrometer (TIS) and a radiometer (TIR), which operate in the wavelength regions of 7-14 µm and 7-40 µm, respectively. This wavelength region is characterized by several diagnostic spectral signatures: the Christiansen feature (CF), Reststrahlen bands (RB), and the Transparency feature (TF), which will allow us to identify and map rock-forming silicates, sulfides as well as other minerals. Thus, the instrument is particularly well-suited to study the mineralogy and composition of the hermean surface at a spatial resolution of about 500 m globally and better than 500 m for approximately 5-10% of the surface. The instrument is fully functional onboard the BepiColombo spacecraft and exceeds all requirements (e.g., mass, power, performance). To prepare for the science phase at Mercury, the team developed an innovative operations plan to maximize the scientific output while at the same time saving spacecraft resources (e.g., data downlink). The upcoming fly-bys will be excellent opportunities to further test and adapt our software and operational procedures. In summary, the team is undertaking action at multiple levels, including performing a comprehensive suite of spectroscopic measurements in our laboratories on relevant analog materials, performing extensive spectral modeling, examining space weathering effects, and modeling the thermal behavior of the hermean surface.

**Keywords** Mercury · BepiColombo · MERTIS instrument · Spectroscopy

---

The BepiColombo mission to Mercury
Edited by Johannes Benkhoff, Go Murakami and Ayako Matsuoka

**Electronic supplementary material** The online version of this article (https://doi.org/10.1007/s11214-020-00732-4) contains supplementary material, which is available to authorized users.

✉ H. Hiesinger
Hiesinger@uni-muenster.de

[1] Institut für Planetenforschung, Deutsches Zentrum für Luft- und Raumfahrt (DLR), Rutherfordstr. 2, 12489 Berlin, Germany

# 1 Introduction

The Mercury Radiometer and Thermal Infrared Spectrometer (MERTIS) onboard ESA's/JAXA's BepiColombo spacecraft will make substantial contributions to our understanding of planet Mercury and the early processes in the inner Solar System, including processes that influenced the geologic evolution of Earth. Summaries of our understanding of Mercury are provided by Strom (1997), Solomon et al. (2001), Solomon (2003), Strom and Sprague (2003), Clark (2007), Head et al. (2007), and Rothery et al. (2010, 2020). Key questions about Mercury include: (1) What is the formation process and why is Mercury so dense? (2) What is the surface and interior composition of Mercury? (3) What is the geologic evolution and history of Mercury? (4) What is the interior structure of Mercury? (5) What is the nature of Mercury's magnetic field? (6) What are the composition and origin of volatile deposits?

To answer some of the important questions outlined above, a thermal infrared spectrometer is an excellent choice because this wavelength region offers unique capabilities to characterize the hermean mineralogy and composition and such an instrument has never been flown in orbit around Mercury and even from Earth, only limited low spatial resolution TIR data are available. The scientific objectives of MERTIS can be grouped into four major scientific goals:

1. Study of Mercury's surface composition
2. Identification of rock-forming minerals
3. Mapping of the surface mineralogy
4. Study of surface temperature variations and thermal inertia.

Building on the science goals defined for MERTIS, we have derived scientific performance requirements, which served as guidelines for the instrument development. A detailed description of the science objectives and the instrument performance requirements can be found in Hiesinger et al. (2010). Table 1 in Chap. 2 summarizes the specified targeted performance, the minimal required performance, and how they are related to the specific science goals outlined above.

Because this paper is intended as an update to our previous instrument paper (Hiesinger et al. 2010), in the first part we will describe the technical details of the instrument, its calibration, and operations. The second part will report on some selected scientific results of our accompanying laboratory program. Thus, the paper provides an overview of the technological/scientific progress made since the publication of the first instrument paper (Hiesinger et al. 2010).

# 2 The MERTIS Instrument

## 2.1 Instrument Description

The Mercury Radiometer and Thermal Infrared Spectrometer (MERTIS) (Fig. 1) is part of BepiColombo's Mercury Planetary Orbiter (MPO) payload and consists of a push-broom IR-spectrometer (TIS) and a radiometer (TIR) (e.g., Hiesinger et al. 2010). MERTIS-TIS and MERTIS-TIR make use of the same optics, instrument electronics, and in-flight calibration components (Hiesinger et al. 2010; Arnold et al. 2010; D'Amore et al. 2018). MERTIS-TIS operates at wavelengths of 7–14 µm, has 78 spectral channels, and a spectral resolution of up to 90 nm. Depending on surface characteristics, we can adapt the spectral resolution

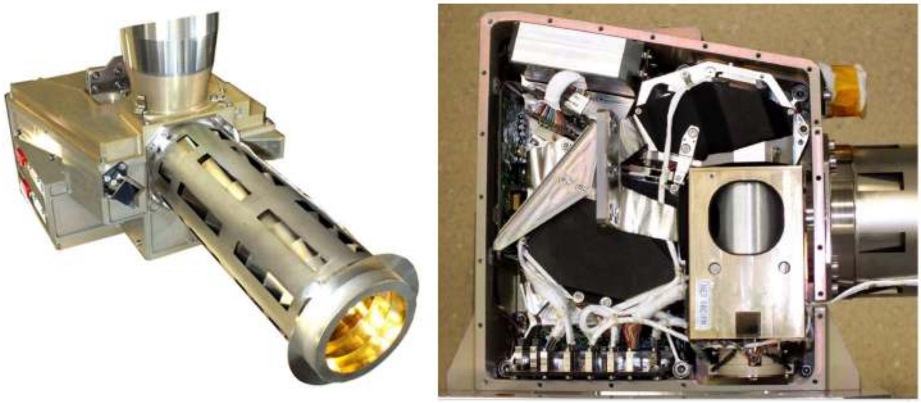

**Fig. 1** The flight model (FM) of MERTIS: View of the ~20 cm long gold-plated planet baffle and the short space baffle (left); top view of interior showing the pointing unit, optics, and wiring (right)

of MERTIS to optimize the signal-to-noise ratio. Thus, the instrument is capable of resolving weak spectral bands of the regolith with less than 1% contrast. MERTIS-TIS data will globally cover Mercury with a pixel scale of 500 m and 5–10% of the planet with a better pixel scale, i.e., better than 500 m. The MERTIS radiometer (TIR) operates at wavelengths between 7 and 40 µm with two spectral channels. The TIR consists of a 2 × 15 elements thermopile double line array sensor chip with an integrated optical slit for the spectrometer and is located at the focal plane of the Three Mirror Anastigmat (TMA) entrance optics.

MERTIS is an uncooled diffraction grating spectrometer. Its optics design consists of a TMA telescope with a focal length of 50 mm, a F-number of 2, and a field of view (FOV) of 4°. The MERTIS spectrometer is based on a modified Offner grating spectrograph. The TMA has three off-axis aspherical mirrors with the second one as aperture stop, whereas the Offner spectrometer uses two concentric spherical elements with a convex grating element opposed by a large concave mirror. This combination is free from spherical aberration, coma, and distortion.

MERTIS utilizes an uncooled micro-bolometer array. This array (produced by ULIS) has dimensions of 160 × 120 pixels, with an individual pixel size of 35 µm. To avoid thermal effects of the main electronics on the detector core, the sensor head with the proximity electronics, and the main electronics with the controlling, interface and power units, are separated. Apart from planet Mercury, MERTIS will sequentially observe three calibration targets – deep space, a 300 K (BB3) as well as a 700 K (BB7) black body. In order to achieve this, MERTIS has a pointing unit, which consists of a single rotary mechanism with a 45° tilted mirror.

The linear performance of the detector depends on its temperature. Thus, temperatures need to be carefully adjusted by a thermo electric cooler (TEC) with a regulation algorithm that stabilizes the detector temperature to 10 mK within an interval of 20–40 °C. To assure thermal stability better than 0.05 °C/min for the detector head, the instrument is mounted close to the radiator of the MPO with the nadir view thermally protected by a baffle.

Technical resources like mass and power consumption are strongly limited for almost all space projects. The imaging spectrometer MERTIS has a mass of 3068.5 g and a power consumption of 9.9–12.4 W. One of the main aspects for the selection of MERTIS by ESA was its small resource consumption with respect to mass and power as well as an excellent optical performance. Thus, the development of MERTIS required a miniature design and several new technologies to be qualified starting from technology readiness level (TRL) 2–5 to finally reach TRL 9 for the flight model (FM) (Peter et al. 2013). Thus, we decided to implement a classical full model philosophy, including a breadboard model, a development model (DM), an electrical model (EM), and a complete qualification model (QM) to qualify the flight design before integrating the flight model (FM). On the basis of these models, we were able to ensure that the main instrument requirements were fulfilled two years before freezing the FM design.

From a financial point of view, the MERTIS advanced model philosophy, especially the early development of the DM, prevented exceeding the budget (Peter et al. 2013). In addition, both mass and power could be further minimized during the final implementation phase while at the same time, the optical performance could be improved.

## 2.2 Instrument Performance and Calibration

To accomplish the defined MERTIS science objectives necessitates meeting the performance requirements summarized in Table 1 (also see Hiesinger et al. 2010). However, due to the fact that our knowledge about Mercury and its surface composition is extremely limited, the requirements were difficult to quantify. To completely fulfill the MERTIS science goals, i.e., to 100% in all aspects, the instrument has to reach the target performance. If only the minimum performance is reached, the achievement of one or several science goals might be affected, but MERTIS will still be capable of achieving the majority of its goals. The requirements on spatial resolution (No. 4, 5, 6, 9) are realized by the MERTIS optical design based on the current orbit scenario and requirements 7 and 10 on coverage are currently fulfilled based on the proposed operational scenario.

We implemented and performed several test and calibration procedures during the instrument development phases. Generally, the MERTIS calibration plan consists of the following parts: (1) ground calibration, which was partly coupled with the optical adjustment, radiometric and spectral stability measurements, and vacuum chamber tests, (2) spacecraft (S/C) calibration for the instrument alignment, and (3) in-flight calibration. The ground calibration included following activities: (1) radiance measurements, (2) wavelength calibration, (3) field of view characterization, and (4) point spread function (Hiesinger et al. 2010; D'Amore et al. 2018; Maturilli et al. 2018).

### *2.2.1 Performance During the Near-Earth Commissioning Phase (NECP)*

The Near-Earth Calibration Phase (NECP) started a few weeks after launch, first commissioning all the spacecraft modules and then the scientific instruments. Details of the MERTIS NECP activities are discussed in D'Amore et al. (2019), here we only give a summary of the key results.

MERTIS' first command was sent on Nov. 13, 2018, 10:51:11 UTC and the instrument was switched off at the end of the last ground station pass on Nov. 14, 2018 16:46:47 UTC for a total operation time of 1 day, 5 hours, and 55 seconds. The operation plan developed for the NECP was aiming to verify the operational performances of all the instrument submodules, in particular the spectrometer and radiometer sensor sensitivities, the pointing unit (MPOI), and the thermal stability of the entire instrument. Once the instrument thermal environment reached its nominal range, the Science_Mode was enabled on Nov. 13, 2018 at 14:16 to 14:56, looking at deep space, acquiring the first MERTIS data ever in space. After that, another 3 data sessions were performed, changing the TIS binning and executing the

**Table 1** MERTIS science performance requirements – green colors indicate that a requirement is fully met

| No. | Sub-Unit | Subject | Target performance | Minimal required performance | Related to science goal |
|---|---|---|---|---|---|
| 1 | Spectrometer | Spectral range | 7–14 µm | 7.2–13 µm | 1,2 |
| 2 | Spectrometer | Spectral resolution | 90 nm | 200 nm | 1,2 |
| 3 | Spectrometer | S/N ratio at Christiansen feature (7.5 µm) | >200 | >100 | 2 |
| 4 | Spectrometer | Spatial resolution at 400 km apoherm | <300 m | <500 m | 2,3 |
| 5 | Spectrometer | Spatial resolution for global mapping | <500 m | 500 m | 2,3 |
| 6 | Spectrometer | Coverage with 500–1000 m resolution | 100% | 95% | 2,3 |
| 7 | Spectrometer | Coverage with better than 500 m resolution | 10% | 5% | 2,3 |
| 8 | Radiometer | NETD at 100 K surface temperature | ≤1 K | ≤3 K | 4 |
| 9 | Radiometer | Spatial resolution at 400 km apoherm | ≤2000 m | ≤5000 m | 4 |
| 10 | both | Operation period | Continuous operation with priorities according to observation conditions | Operation during the periherm on dayside | 3 |

normal operation/calibration cycle of 60 seconds: “Cold” 300 K blackbody (BB3), “hot” 700 K blackbody (BB7), deep space, and planet view.

The latter position is currently obstructed by the Mercury Transfer Module (MTM) structure and will be freed after Mercury orbit insertion. The acquired measurements will be used as further calibration, after the temperature of the obstructing MTM portion has been accurately modeled. This modeling is necessary because there is no thermal sensor directly in the MERTIS planet view field of view, so the closest spacecraft thermal data must be collected and interpolated. In each measurement session, a TIS acquisition took 100 milliseconds, plus the time to rotate the MPOI to different positions. The instrument was left switched on at the end of the first day session and in thermally stable condition during the night to start with a highly stable thermal condition on the 2nd day. The second day had a similar data operation pattern, with a much higher housekeeping generation rate, each second instead of each 20 seconds, which is the default for the nominal mission. The total amount of scientific data and housekeeping data obtained during NECP is on the order of 1.15 GB, for a total of around 120k TIS and 15k TIR acquisitions.

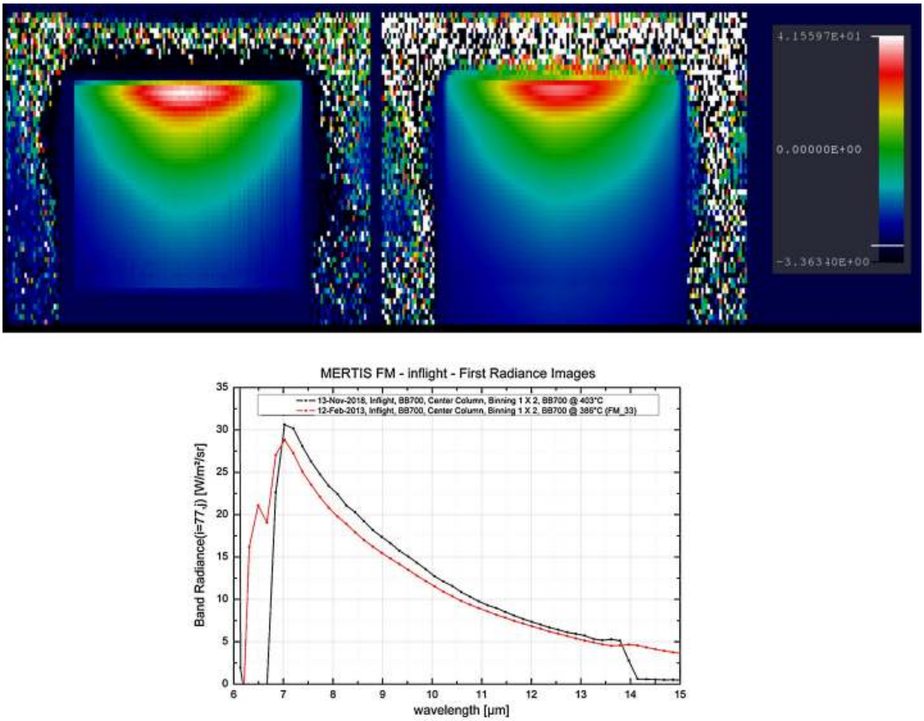

**Fig. 2** Top panel: Radiance values from BB7 blackbody inflight (right) and on-ground (left) [Blue: −3.63 W/m$^2$/sr; Red: 41.56 W/m$^2$/sr]; Bottom panel: BB7 TIS spectral comparison between measurements on–ground and space

The grating spectrometer differential (scene – dark scene) images acquired at different MPOI positions are shown in Fig. 2 The outer parts of the detector are masked because the pixels in these areas only show signal induced by thermal noise. The average value of all masked pixels is an important indicator of the thermal state of the microbolometer itself and of the noise generated at these specific thermal conditions. For all the images the binning was [spatial × spectral] = [1 × 2], resulting in a Spectral Sampling Distance (SSD) of 89 nm. The MERTIS calibration curves have 5 different regimes, depending on the total sensor voltage. During NECP, we were in the OP-Point 2. The top panel of Fig. 2 shows the radiance values for the BB7 in-flight (right) and on-ground (left), the bottom panel shows spectral curves extracted from the center of the BB7 images. From this, we conclude that the MERTIS TIS spectrometer channel is fully functional after launch. The MERTIS in-flight performance is comparable with our last measurements on-ground with only a very small image shift after launch ($<$0.5 pixel). Slight changes in the parameters for the analog-digital converter (ADC) were observed, so adjustments of working points are being performed. Further details are discussed in D'Amore et al. (2019).

While the on-ground and in-flight measurements for TIR radiometer broadband channel A (8–14 µm) are basically identical, we observed a slight sensitivity decrease of the TIR radiometer broadband channel B (5–40 µm) by 12%. However, this was already known from our on-ground measurements before launch. Figure 3 shows a comparison of the BB7 signal measured by the radiometer on-ground and in-flight (left for the 7–14 µm channel and right for the 7–40 µm channel). Thus, the MERTIS-TIR radiometer channel is fully

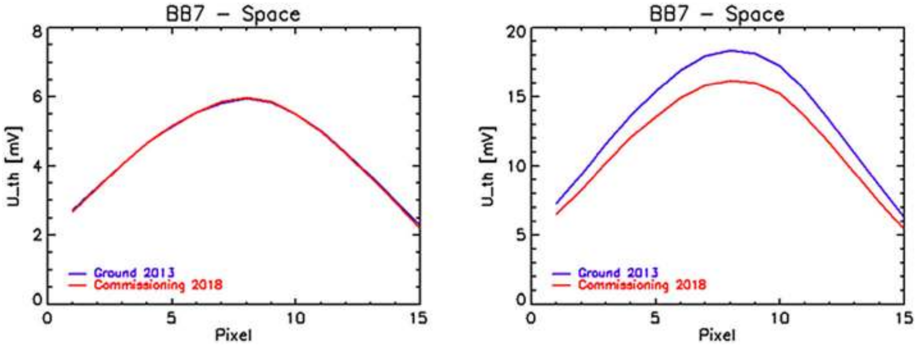

**Fig. 3** Radiometer measurements during NECP: left panel: BB7 – Space [IR-A 8–14 μm] right panel: BB7 – Space [IR-B 5–40 μm]

functional after launch, with a slight degradation in the long wavelength channel. In general, noise performance determined from the standard deviation of the difference between BB3 and space view, containing electronics and thermal noise, is unchanged. In summary, the in-flight calibration of MERTIS provides a means to track and correct changes in the sensitivity of the radiometer. Details are discussed in D'Amore et al. (2019)

### 2.2.2 Archival Data Format

The final archival data format has been developed in collaboration with the European Space Agency Science Ground Segment (ESA/SGS). We follow NASA Planetary Data System (PDS4) standards that ensure automatic integrity checks against semantic dictionaries, defining type and acceptable range for each data element. The PDS4 format enforces the use of XML labels describing the allowed physical data format. The TIS and TIR data, with all accompanying metadata and housekeeping data (HK), are physically stored in the Flexible Image Transport System (FITS) and American Standard Code for Information Interchange (ASCII) formats. This ensures automatic data quality checks during the data creation stage. FITS is an open standard defining a digital file format optimized for storage, transmission, and processing of data; formatted as multi-dimensional arrays (for example a 2D image), or tables. FITS is the most commonly used digital file format in astronomy, was designed specifically for astronomical data, and includes provisions such as describing photometric and spatial calibration information, together with image origin metadata. ASCII is a character-encoding standard for electronic communication that represents text in computers, telecommunications equipment, and other devices, ensuring long-term readability and quick interaction with the data.

MERTIS produces a constant stream of HK data (default and extended) with a variable rate that is adjusted to match the instrument environmental condition: A higher data rate is used for periods with known high thermal fluctuation. This is needed to constrain the instrument observation condition during measurements, which is necessary for the accurate calibration of the data. The housekeeping data are stored as simple ASCII matrix and will be available for download and quick visualization at the ESA's Planetary Science Archive (PSA). There are several options to interact with PDS4 and FITS for which the MERTIS team is developing Python PDS4 Tools and the Astropy package FITS interface. The data produced by MERTIS per acquisition are summarized in Table 2.

**Table 2** Summary of the data produced by MERTIS channels for each acquisition

| TIS Spectrometer | TIR Bolometer |
|---|---|
| Metadata<br>(i.e., sensor pixel sampling) | Metadata<br>(i.e., internal blackbody temperature) |
| Sensor 2D Frame<br>(spectral × spatial pixel) | A and B channels for 7–14 µm and 7–40 µm<br>(15 spectral pixels per channel) |

### *2.2.3 Operations: General Remarks*

The MPO will have a 2.3-hour polar orbit with the periherm located above the equator at an altitude of 480 km and the apoherm at 1500 km altitude. This orbit configuration, together with a FOV of the instrument of 4°, yields subsequent ground tracks that will overlap at least 10% at the equator and even more in the polar regions. During the mission, MERTIS will be operated continuously.

Instrument operations in the challenging environment at Mercury with power and data constraints require a sophisticated mapping scheme for the TIS observations, which also has to account for the MERTIS calibration needs. Execution of this scheme creates challenges for the operation of the instruments, data processing, and the creation of map products. Extensive on-ground testing and rehearsals during the Earth and Venus fly-bys will facilitate operations at Mercury (also see Maturilli et al. 2018).

### *2.2.4 Instrument Check-out Plan During Cruise*

During the cruise phase, we perform a checkout procedure once every six months. These tests are identical to the tests performed during the NECP. At the end of August 2019, the cruise checkout period was used to successfully test the operational scenario for the fly-bys, i.e., observing through the space baffle.

### *2.2.5 Planetary Fly-Bys*

BepiColombo will have one fly-by at Earth/Moon, two fly-bys at Venus, and six fly-bys at Mercury before entering orbit around Mercury. Although most instruments are blocked by the MTM, including the MERTIS planet baffle, MERTIS will be able to acquire data through its space baffle. We already adapted the MERTIS operations software to take advantage of these unique opportunities. In particular, the Earth/Moon fly-by is of interest, as the surface composition of the Moon and Mercury have been frequently compared in the literature (e.g., McCord and Clark 1979; Vilas 1988; Robinson and Lucey 1997; Blewett et al. 1997; Warell 2002, 2003; Warell and Blewett 2004). Observing the Apollo and Luna landing sites with MERTIS, in combination with laboratory studies, would provide extremely valuable ground truth for our MERTIS measurements. However, the spatial resolution during the fly-by was limited to about 6–7 pixels (∼500 km pixel scale on the surface), which still allows us to recognize differences between mare and highland regions. MERTIS is the first instrument to observe the Moon in this wavelength range from space.

The current database of Venus in the TIR spectral region is very limited. The only comparable data set was acquired by the Venera 15 mission in 1983 (Oertel et al. 1985). Although the JAXA mission Akatsuki acquires observations from 0.283-10 µm region (Nakamura et al. 2007), it misses most of the $CO_2$ band centered around 15 µm. In addition, Akatsuki's orbit results in changing viewing geometries of Venus, complicating the studies of its whole-disk brightness. Because Akatsuki is unable to perform spectroscopic observations, it cannot investigate several atmospheric depths simultaneously. MERTIS, however, will allow us to investigate several atmospheric depths at the same time. To do so, we will perform simultaneous observations with the spectrometer and the radiometer channel and using the internal BB3 for calibration. The science mode will be optimized with respect to binning and dwell time to maximize the signal-to-noise ratio. The two Venus fly-bys offer us the opportunity to gather scientific data from Venus for more than 60 minutes, using various science modes.

All these fly-bys require a special operational procedure. Thus, we developed a planetary fly-by mode during which calibration sequences will be obtained before and after the fly-by while during the fly-by only science frames will be acquired. The macropixel parameters and the repetition times will be defined based on limitations set by spacecraft resources, to reduce data volume and power consumption.

### *2.2.6 Near-Mercury Commissioning Phase*

After arrival at Mercury, the Near-Mercury Commissioning Phase will consist of two phases to fully assess the operational performance of the instrument. First, we will verify the instrument functionality and basic instrument performance. This will be done following identical operation procedures as for the NECP, making use of the inflight calibration devices and verifying their performance. After switching on the instrument, we will test a nominal science mode for several hours, followed by a diagnostic mode to verify the sub-system functions of MERTIS. During this test, we will execute several operation modes for MERTIS (approx. 30 minutes each) to test the instrument response.

Second, we will perform a full operational verification of the instrument performance. BepiColombo will enter orbit during Mercury's summer season (perihelion; see Fig. 4). After verification of the instrument functionality and performance, MERTIS will perform a sequence of observations for several orbits following the general procedures for the survey mapping.

### *2.2.7 MERTIS Operations in Mercury Orbit*

In order to achieve the MERTIS goal to globally map the mineralogy of the hermean surface at a pixel scale of better than 500 m, the baseline operation for MERTIS is continuous mapping. However, severe limitations in mission resources require an optimization of instrument operations. Although MERTIS could theoretically completely cover the surface after two Mercury years, data gaps due to the calibration cycle will need to be filled during the third and fourth Mercury year, which will have identical illumination as the first two years. Thus, it will take MERTIS the entire mission time to complete the mineralogical map at highest spatial resolution. MERTIS operations will follow Mercury's seasons (see Fig. 4) such that during winter (aphelion), the periherm of the spacecraft orbit will be on the dayside. This is the time in which MERTIS will perform high-resolution mapping at pixel scales of $<500$ m. During summer (perihelion), the periherm will be on the nightside. During that time, MERTIS will perform survey mapping. Because this period will provide best conditions for radiometric observations, MERTIS will map the temperature at highest spatial resolution. The dayside perihelion passes will yield data with low spatial resolution and TIS observations will mainly be used for planning of the next aphelion period.

Mercury's surface temperatures vary greatly with season. Thus, performing temperature measurements for the same region at different times will allow us to better constrain the

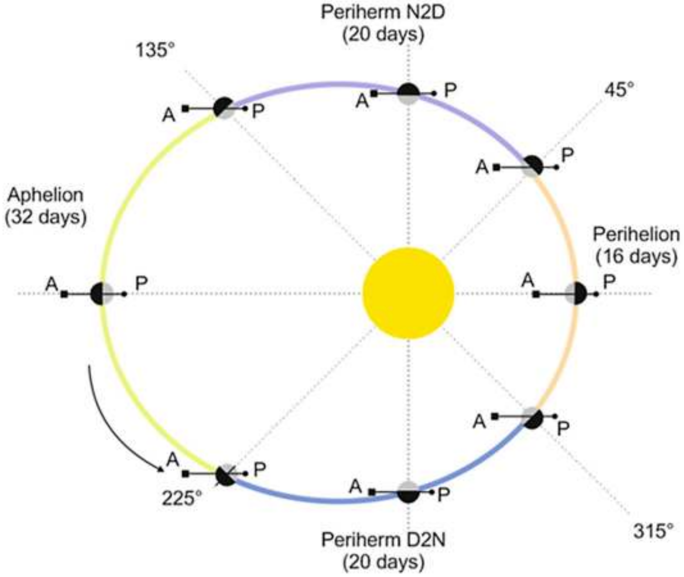

**Fig. 4** MERTIS operations during a Mercury year (A=Apoherm, P=Periherm). Colors indicate mission phases (Tan=Survey Mapping, Green= High-Resolution Mapping, Blue/Purple= Thermophysical/Polar Mapping)

thermophysical properties and mineralogy by retrieving information on the temperature dependence of the surface emissivity. Furthermore, the changing viewing conditions between the mapping phases provide additional insight into phase-dependent surface properties.

BepiColombo's orbit will be close to the terminator during spring and autumn and these are the least favorable observation conditions for MERTIS, although the strong and rapid temperature changes around sunrise and sunset will provide the highest contrast in surface radiance. In this period, MERTIS will perform thermophysical and polar mapping. The data obtained enable us to constrain models of the physical properties of the regolith and to measure temperature differences between permanently shadowed craters and the surrounding plains.

**High-Resolution Mapping** The amount of overlap of MERTIS data depends on two factors: The swath width as a function of target distance and the ground track spacing of consecutive orbits.

Due to the characteristics of the orbit and the FOV of MERTIS, the overlap is increasing quickly with spacecraft altitude and therefore angle from periherm (Fig. 5). The overlap (in %) can be calculated as

$$over = ((sw - orb\_st)/orb\_st * 100)$$

where $sw$ is the swath width and $orb\_st$ is the spacing between consecutive orbits at this point.

For example, for an overlap of 110% between orbit $n$ and orbit $n+1$, the MERTIS data obtained at the angle from periherm in orbit $n+1$ are redundant because the same area is covered in orbits $n$ and $n+2$. In an ideal scenario, these redundant data would allow increasing the signal-to-noise of the instrument and radiometric cross calibration of orbits.

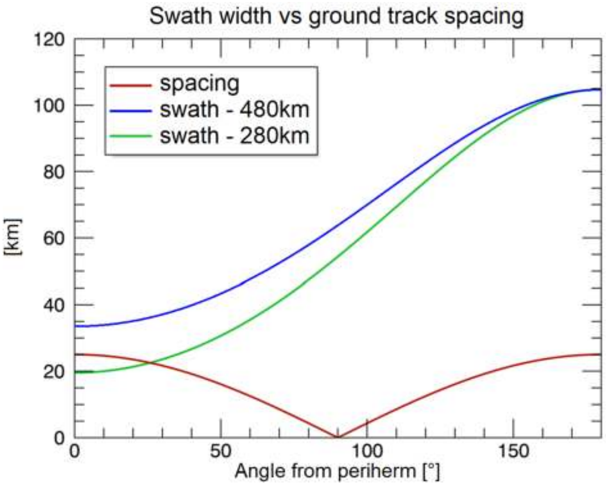

**Fig. 5** MERTIS swath width and track to track spacing (red) vs angle from periherm during the high-resolution mapping phase, assuming periherm at 280 km (green) and 480 km (blue). Notice that for periherm at 280 km, the swath width is smaller than the track spacing below 30° from periherm

However, the limited resources of the mission do not allow downloading the additional data. Hence, the operational scenarios have been optimized to minimize the overlap while guaranteeing the necessary calibration data.

We apply a simple calculation to help guiding MERTIS operations, i.e., if the overlap between orbits $n$ and $n+1$ exceeds $M * 100 + 10\%$, the next $M$ orbits will be skipped. This implicitly assumes that the orbits are stable over the period of $M$ orbits and that the spacecraft is in nadir pointing configuration. If the MPO is off nadir this has to be taken into account in calculating the orbit. It also implies that MERTIS is observing in orbit $n + M$, otherwise half of the area between orbit $n$ and orbit $n + M$ is not covered even if MERTIS is operated until orbit $n + M - 1$.

This simple rule already eliminates a significant amount of redundant observations, thereby reducing the overall data volume that has to be downlinked. The simple rule does not allow for an optimization if the overlap is below 110%. MERTIS cannot skip one orbit as this would cause a data gap. However, there is still overlap between the consecutive orbits. In order to further optimize the observing strategy, a window mode is implemented in the flight software, which allows to readout only the central 70% of the detector array. Extending the above rule, this mode is implemented once the overlap exceeds 80%.

As discussed before, the swath width is a function of the periherm distance of the orbit and the angle from periherm. In an extreme scenario where the "skip" rule was applied along a 180° arc of the orbit, the periherm is over one of the poles of Mercury. In this case we have a minimum of six changes along the orbit. In general, while MERTIS is in operational mode, the telecommands Science_Enable and Science_Disable are used to start and stop an observation. We will perform a switch to MERTIS_TIR_only mode for the evening terminator pass and the switch back to TIR and TIS mode for the morning terminator. This results in a total of at least eight telecommands (TCs) within the MERTIS timeline for one orbit – compatible with the limit of ten TCs per orbit imposed by the European Space Operations Centre (ESOC).

Extending the skipping beyond four orbits increases the complexity significantly, especially for the mosaicking of the received data, without significant further reduction in data volume, as can be seen in Fig. 6.

Figure 7 schematically shows the sequence for 10 consecutive orbits. Colored lines indicate that MERTIS is taking data; the dashed lines indicate that the windowing mode is used.

**Fig. 6** Application of the "skipping" rule to a MPO orbit with periherm at 480 m

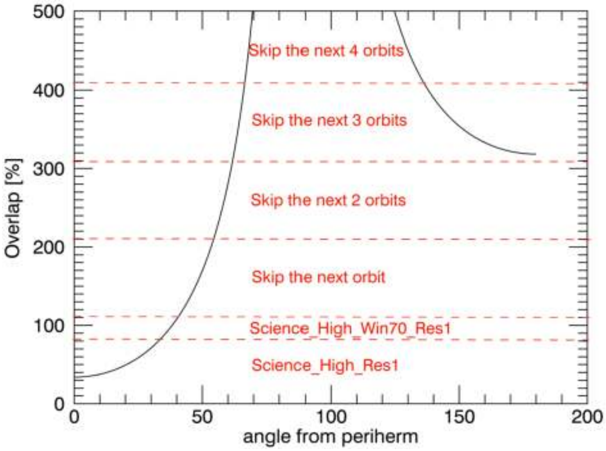

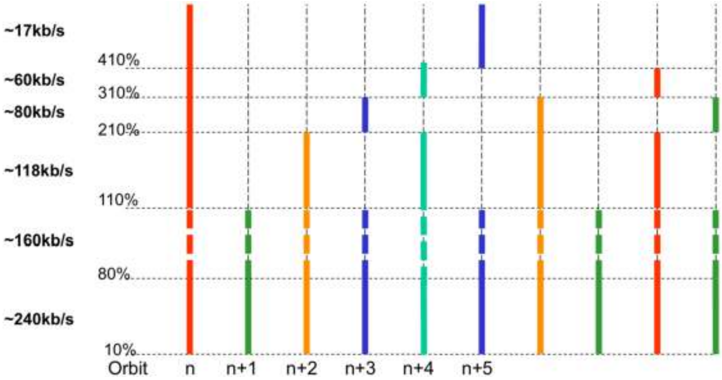

**Fig. 7** Schematic display of the operational sequence over a period of 10 orbits

Beyond 410% overlap no further optimization is performed to limit the amount of mode switches during an orbit. The data rates given for each latitude range are averaged for the entire sequence.

Using the simple rule given above, this scenario could be extended continuously. The sequence would repeat after approximately 60 orbits. However, given the caveats discussed before about the importance of orbital stability during the sequence in order to allow skipping orbits without losing coverage, the MERTIS team proposed to limit the sequence to 10 orbits. The n+11 orbit would then again be a full orbit. These full orbits are the preferred candidates for the 10% flexible downlink of MERTIS data.

Of course, this timeline for the MERTIS operation depends on the orbit geometry. Tables 3, 4, and 5 in the supplementary materials show examples for three different orbit configurations and the effects on MERTIS operations.

**Survey Mapping and Radiometry** The survey mapping mode of MERTIS follows a similar sequence than the high-resolution mapping mode (Fig. 8). However, due to the larger spacecraft/surface distance during the dayside passage, the spatial resolution will be reduced and the largest overlap will occur close to the equator and will be smaller toward higher latitudes.

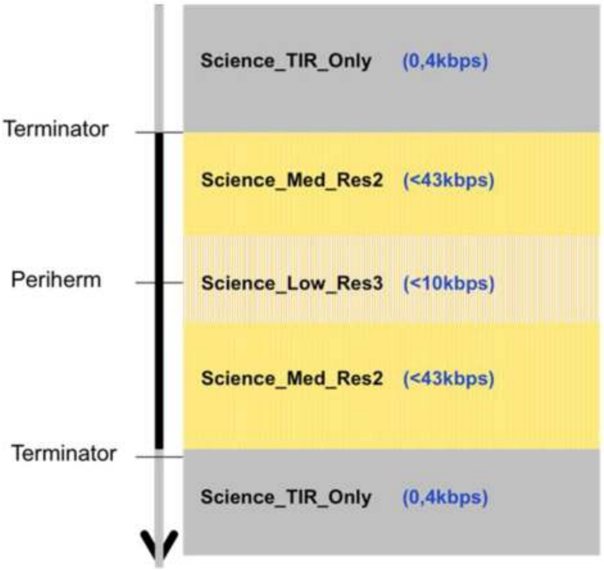

**Fig. 8** Operational scenario during the survey mapping phase with maximum data rates based on sequencing

**Thermophysical and Polar Mapping** During the thermophysical and polar mapping phases, we will apply a different approach than for the high-resolution and the survey mapping modes (Fig. 9). Whereas the latter two are focused on global mapping, the thermophysical and polar mapping phase will take advantage of the special illumination and observing geometries in the autumn and spring dusk-dawn orbits to obtain observations with maximal thermal contrast. This mode will allow us to investigate in detail the thermophysical properties of small surface regions on Mercury and will also provide data of polar regions with a high signal-to-noise ratio by stacking observations. Such stacking is necessary because surface temperatures close to the poles of Mercury approach the sensitivity limit of MERTIS. In the polar regions in particular, we will acquire low- and high-resolution data to combine the benefits of high signal-to-noise with high spatial resolution measurements, while at lower latitudes, we will acquire mostly low-resolution data to maximize the signal-to-noise for thermophysical measurements.

**Other Modes / Characterization Mode** While MERTIS will operate in the high-resolution mapping mode mainly during winter and in survey mapping mode during summer, additional modes can be operated during various seasons. For example, the characterization mode will be used to characterize the instrument function and performance. During the commissioning phase and also periodically during the operation phase, we plan to collect mainly calibration frames at full spectral and spatial resolution over an extended period of time because it will allow us to determine the long-time stability of the instrument, identify possible thermal drifts, as well as study possible degradations of the instrument performance. In combination with other instruments, the characterization mode will provide an interference test, i.e., how MERTIS operations might affect other instruments such as the magnetometer.

### *2.2.8 MERTIS In-Flight Calibration and Nominal Operations*

The three MERTIS in-flight calibration sources (BB3, BB7, deep space view as proxy for zero-radiance) will be periodically observed during the regular science acquisition procedure

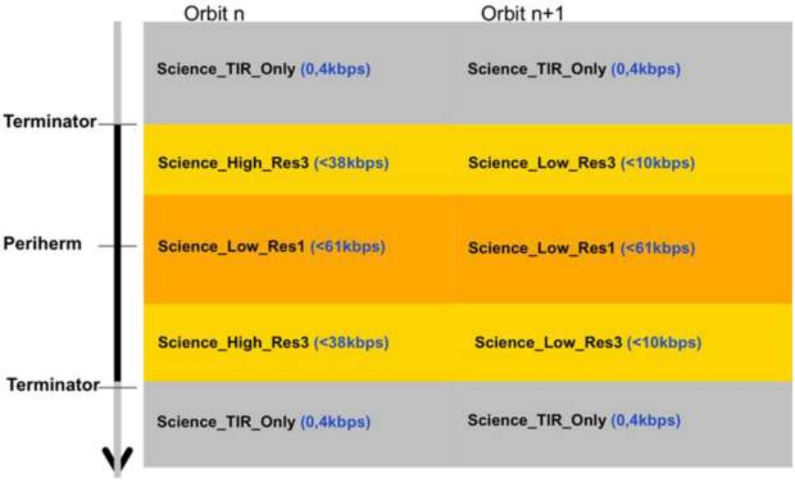

**Fig. 9** Two orbit sequence in the thermophysical and polar mapping phase

and do not require special S/C commanding. As a result, MERTIS will produce calibration data at the same spatial and spectral resolution as the science data.

Depending on the position of Mercury along its orbit, operations of MERTIS will be adapted. Nominal operations during the dayside pass in the high-resolution mapping mode will yield continuous push-broom observations with alternating sciences and calibration frames. One complete calibration and observation cycle will take about 20 s (Fig. 10). During this time, the pointing unit will rotate 360°, observing the hermean surface for 13 s and the BB7, BB3, and cold space for 1 s. In between each observation, there will be start/stop times of 1 s each. We plan to fill the gaps that are caused by the calibration of the instrument in later orbits. During the periherm passage where the spacecraft has the highest ground velocity, we can suspend the calibration cycles.

Nominal operations during the nightside pass in the survey mapping phase foresee a continuous operation of the radiometric channel of MERTIS with calibration cycles in to-be-determined intervals. For the radiometric observations on the nightside, MERTIS will only use the BB3 and the deep space view and we will use macropixel binning to increase the signal-to-noise ratio and to reduce the data rate (e.g., Maturilli et al. 2018). We define macropixel as the averaged noise of the sensor area that is not exposed to incoming light. This gives us the level of thermal noise produced during the observation.

## 3 Science

To avoid redundancy with our earlier summary paper (Hiesinger et al. 2010) and the companion paper by Rothery et al. (2020), which both describe in detail the hermean geology and possible MERTIS contributions, we only repeat several major points.

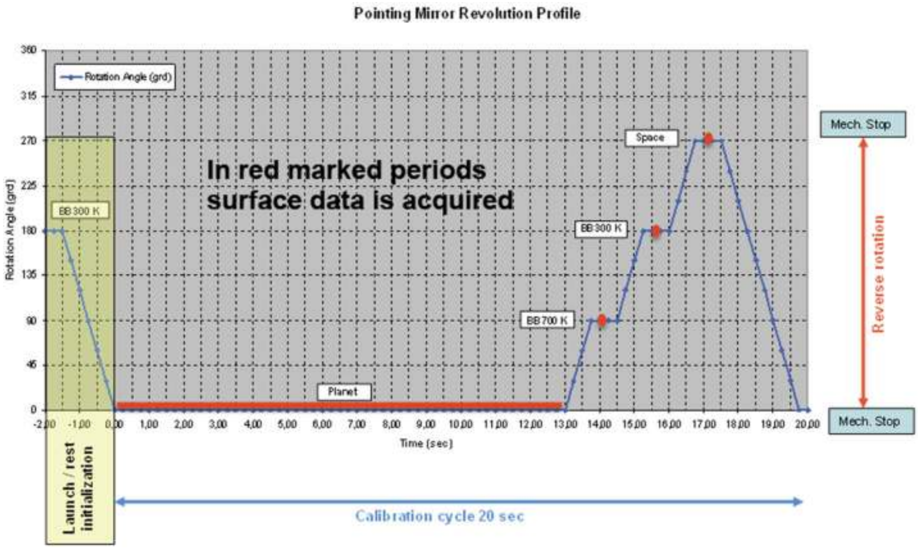

**Fig. 10** MERTIS calibration cycle during nominal operations

## 3.1 Scientific Questions Relevant to MERTIS

### *3.1.1 The Origin of Mercury*

Several hypotheses for Mercury's unusually high density have been put forward and each of them makes specific predictions concerning the composition of surface rocks. Thus, we will be able to verify/falsify these model predictions and by that learn about Mercury's interior by studying the composition and mineralogy of the hermean surface with MERTIS. These models include, for example, aerodynamic fractionation during the accretion phase (Weidenschilling 1978), a giant impact that stripped off the primordial crust and upper mantle (Benz et al. 1988; Cameron et al. 1988; Wetherill 1988; Benz et al. 2007), differential evaporation of elements during the Sun's early T-Tauri phase (Cameron 1985), refractory condensation as a consequence of a steep temperature gradient in the solar nebula (Lewis 1972, 1974), refractory-volatile models, which consider mixing throughout the inner Solar System (Goettel 1988; Morgan and Anders 1980), and partial melting of chondritic material (Wasson 1988; Burbine et al. 2002; McCoy et al. 1999).

### *3.1.2 The Surface Composition of Mercury*

Although difficult to accomplish, Mercury has been observed multiple times with ground-based telescopes (e.g., Harris 1961; Moroz 1965; Irvine et al. 1968; McCord and Adams 1972; Vilas and McCord 1976; Vilas et al. 1984; Vilas 1985, 1988; Sprague et al. 1994, 2002; Emery et al. 1998; Cooper et al. 2001; Warell and Blewett 2004; Ksanfomality et al. 2007). Although early ground-based observations did not detect absorption features in the VIS-NIR spectral range (e.g., McCord and Clark 1979; Vilas et al. 1984; Warell and Blewett 2004), Warell et al. (2006) attributed weak absorption features to $Fe^{2+}$

in high-Ca clinopyroxene and concluded that Mercury's surface is heterogeneous and exhibits an iron-poor mineralogy.

The wavelength positions of thermal emissivity maxima are consistent with intermediate or slightly mafic rock types and a non-homogeneous surface composition (Tyler et al. 1988; Sprague et al. 1994, 1997). Specifically, variations in modal abundances of albite and in the composition and abundance of pyroxenes have been observed (Tyler et al. 1988; Sprague et al. 1994, 1997; Sprague and Roush 1998) and some locations with ultramafic compositions have been identified Cooper et al. (2001). In addition, a Mercury spectrum obtained at $\sim 34°$ was found to be similar to spectra from Apollo 16 breccias although the Mercury spectrum indicates higher Na contents of the feldspars (Sprague and Roush 1998).

Mercury's surface further undergoes extreme temperature cycles from about $-150\,°\mathrm{C}$ (midnight) to $450\,°\mathrm{C}$ (noon) unlike any other planetary body in the Solar System. This leads to thermal weathering of surface materials, which further affects the nature of material and their spectral properties (Helbert et al. 2013a, 2013b; Maturilli and Helbert 2014; Maturilli et al. 2019; Maturilli et al. 2017; Varatharajan et al. 2019a). MERTIS will map the surface mineralogy along with its surface temperature. This unique dataset will further help us to understand the real-time effects due to temperature, micrometeorites, and solar-wind radiation on Mercury's surface.

### *3.1.3 Volcanism and the Interior of Mercury*

The composition of volcanic deposits serves as a proxy for the composition of the planet's interior. Thus, we are interested in the question whether the interior, i.e. the mantle, is similarly depleted in FeO as the surface (2–3 wt.%) (Robinson and Taylor 2001). According to MESSENGER results, the average total iron on the surface of Mercury is less than 2.4 wt% (Nittler et al. 2011; Evans et al. 2012; Weider et al. 2014; McCoy et al. 2018). On Mercury there are two plains units, an older intercrater unit and a younger smooth plains unit that have been interpreted to be lava flows, i.e., to be of volcanic origin (e.g., Murray 1975; Murray et al. 1975; Trask and Strom 1976; Adams et al. 1981; Rava and Hapke 1987; Spudis and Guest 1988; Robinson and Taylor 2001; Milkovich et al. 2002; Byrne et al. 2018; Denevi et al. 2018, and references therein). However, TIR emission spectra of Sprague et al. (1994) are also consistent with a surface that is dominated by feldspar (plagioclase) (Jeanloz et al. 1995), an interpretation supported by spectral similarities to the lunar highlands (Blewett et al. 2002; Warell 2003; Warell and Blewett 2004). Although this is consistent with an impact origin of the plains, MESSENGER found evidence for a volcanic origin of smooth plains and also identified numerous pyroclastic features (Kerber et al. 2009; Goudge et al. 2014; Thomas et al. 2014; Byrne et al. 2018, and references therein). Detailed analyses of surface spectra in the TIR part of the electromagnetic spectrum obtained by MERTIS will provide further insights into the volcanic history and evolution of Mercury.

Several models have been developed to explain the existence of the hermean magnetic field (e.g., Srnka 1976; Stephenson 1976; Christensen 2006; Christensen et al. 2006). One of these models proposes a dynamo-generated magnetic field attenuated by an upper stably stratified liquid core (Christensen 2006; Christensen et al. 2006). This requires a mechanism to stop Mercury's core from completely freezing and such a mechanism might be the dissolution of low melting-point elements like sulfur or oxygen (Schubert and Spohn 1990; Harder and Schubert 2001; Spohn et al. 2001). With MERTIS, we will search for volatile elements like sulfur in sulfur-containing compounds to test and further constrain the geophysical models of the interior of the planet.

### 3.1.4 Volatiles of Mercury

Despite the fact that Mercury is the planet closest to the Sun, it is unusually rich in volatiles (Nittler et al. 2018, and references therein). Several lines of evidence for volatiles exist, including a high potassium/thorium ratio, radar bright polar deposits, and hollows interpreted as regions of volatile loss. On the basis of MESSENGER data, Ebel and Stewart (2018) found that Mercury is enriched in S, Na, and Cl. Highly reflective deposits seen in radar data were interpreted as cold-trapped water ice (Harmon and Slade 1992; Slade et al. 1992; Butler et al. 1993; Harmon et al. 1994; Killen et al. 1997), elemental sulfur (Sprague et al. 1995) or silicates at very low temperatures (50–80 K) (Starukhina 2001).

Observations with MESSENGER's (Leary et al. 2007) Mercury Dual Imaging System (MDIS) and X-Ray Spectrometer (XRS) indicate a generally volcanic surface with high abundances of magnesium, calcium, and sulfur (up to 4 wt.%) (Nittler et al. 2011). Global scale results from the XRS instrument (Weider et al. 2012) indicate a correlation between the calcium and sulfur abundances, hinting at the potential presence of calcium sulfides.

Low reflectance material identified in the ejecta of some large basins might be evidence for a graphite-rich layer that formed as a result of magma ocean crystallization under hermean P/T conditions (Brown and Elkins-Tanton 2009; Vander Kaaden and McCubbin 2015; Peplowski et al. 2016, Klima et al. 2018).

Mariner 10 (Dzurisin 1977) and MDIS observations showed that bright and spectrally blue deposits associated with impact crater floors, central peaks, and wall terraces, are characterized by irregular, shallow, fresh appearing rimless depressions, i.e., hollows (Robinson et al. 2008; Blewett et al. 2009, 2010, 2011a, 2011b, 2018; Rothery et al. 2020). With MERTIS, we will contribute to the ongoing debate about the nature of the deposits in which the hollows form. Sulfides, for example, have been proposed as a possible candidate (Blewett et al. 2011a, 2011b; Vaughan et al. 2012) and these sulfides might have been brought to the surface during volcanic activity (Helbert et al. 2013a). These deposits further undergo decomposition due to extreme temperature conditions and photo-dissociation resulting in the formation of Mercury hollows (Helbert et al. 2013a; Bennett et al. 2016; Killen 2016).

### 3.1.5 Effects of Space Weathering

Compared to the Moon, Mercury's surface is likely more severely altered by space weathering (SW), i.e., the bombardment with micrometeorites and cosmic and solar wind irradiation (Cintala 1992; Noble and Pieters 2003). Thus, we can expect that SW effects, including comminution, formation of glassy agglutinates and nanometer-scale metallic Fe particles (npFe$^0$), are common on Mercury (Trang et al. 2017). Although the hermean surface is generally much poorer in iron than the lunar surface, it has been argued that even for the extreme endmember case where the surface of Mercury has no native FeO, the iron brought in by meteorites should be sufficient to produce significant amounts of npFe$^0$ through vapor fractionation (Noble and Pieters 2003). The formation of npFe$^0$ might also be responsible for the observed remnant crustal magnetization (e.g., Johnson et al. 2015; Strauss et al. 2016). Thus, understanding the effects of space weathering on MERTIS spectra is critical for their accurate interpretation and justifies a comprehensive laboratory program that simulates SW by short-pulsed lasers, ion bombardment, and shock recovery experiments on various minerals and their mixtures (Weber et al. 2019, 2020a, 2020b; Stojic et al. 2019).

### 3.2 Lessons Learned from Diviner

The Diviner Lunar Radiometer Experiment (Diviner) is a nine-channel pushbroom thermal infrared spectrometer onboard the Lunar Reconnaissance Orbiter (LRO) mission, operating in the wavelength region between 0.35 and 400 µm (Paige et al. 2010). Thus, as Diviner covers the same spectral features (CF, RB, TF) as MERTIS, it is of great value to guide our preparatory laboratory work and the accurate interpretation of our MERTIS data. The instrument has three narrow-band filters (7.55–8.05 µm, 8.10–8.40 µm, and 8.38–8.68 µm) that were specifically designed to characterize the CF and has a pixel size of about 200 m on the lunar surface (Greenhagen et al. 2010). Before Diviner, it was thought, that the thermal infrared range is basically insensitive to space weathering (e.g., Nash et al. 1993) and that the position of the CF is only dependent on the chemical composition (Nash and Salisbury 1991; Salisbury et al. 1997). However, this conclusion is inconsistent with Diviner results, which indicate a dependency, for example, on space weathering (e.g., Lucey et al. 2010; Greenhagen et al. 2010; Glotch et al. 2015), albedo (e.g., Shirley et al. 2018; Kumari et al. 2020. Lucey et al. (2017), and grain size (e.g., Shirley and Glotch 2019; Mustard and Hays 1997). It is also inconsistent with modern laboratory spectral measurements under vacuum conditions (e.g., Bramble et al. 2019, and references therein). Thus, deriving mineralogical/compositional information from thermal IR spectra is more complicated than previously thought and requires detailed understanding of these parameters, how they interfere with each other, and how they affect the spectral interpretation.

Lucey et al. (2017) proposed that space weathering effects on the CF position are caused by albedo-dependent variations in the thermal gradient in the uppermost parts of the surface rather than compositional differences in response to processes commonly associated with space weathering (vapor-deposited coatings, agglutinate formation, npFe$^0$ formation). In this respect, it is particularly important to consider the effects of vacuum because the CF position occurs at a wavelength where the real index of refraction of a mineral passes through unity (e.g., Lucey et al. 2017). Vigorous gas conduction at ambient laboratory pressures causes isothermal conditions whereas conduction in vacuum becomes very low because it is restricted to grain-to-grain contacts (e.g., Lucey et al. 2017). As a result, under ambient conditions, a regolith simulant behaves more or less isothermally whereas on airless bodies, a regolith will be warmer beneath the surface compared to the proper surface, an effect known as solid-state greenhouse (Lucey et al. 2017). Compared to an isothermal state, in the presence of a thermal gradient the CF position for bright regions shifts more strongly to shorter wavelengths than for low albedo regions (Lucey et al. 2017). Several studies have documented a shift in the CF position to shorter wavelength, as well as an increase in spectral contrast with decreasing pressures (e.g., Logan et al. 1973). In their thermal and radiative transfer models, Henderson and Jakosky (1997) and Henderson et al. (1996) quantified this shift to be as large as 0.5 µm, depending on the thermal conductivity and grain size. Henderson et al. (1996) pointed out that the conversion of reflectance spectra into emissivity spectra of airless bodies with a thermal gradient (i.e., applying Kirchhoff's law) is inaccurate and should be treated with care.

As discussed above, thermal gradients are dependent on thermal conductivity, which in turn depends on, for example, grain size and porosity. Grain size effects on thermal IR spectra have been investigated by several studies, including Logan and Hunt (1970), Logan et al. (1973), Henderson and Jakosky (1997), Mustard and Hays (1997), and Shirley and Glotch (2019). The latter study performed by Shirley and Glotch (2019) under simulated lunar conditions indicates that smaller grain sizes enhance the spectral contrast of the RB and TF and shift the CF to longer wavelengths. Mustard and Hays (1997) studied grain sizes that were on the order of the incoming light ($<25$ μm). In their bidirectional reflectance spectra, they observed systematic changes: (1) for the finest grain size separates, the reflectance dropped sharply in regions of volume scattering, (2) the CF became saturated when the imaginary part of the refraction index was non-negligible, (3) with decreasing grain sizes, the spectral contrast and shape of the RBs changed, (4) with decreasing grain sizes, the spectral contrast of the TF increased and then decreased, the position of the reflectance maximum of the TF moved to shorter wavelengths, and the symmetry of the feature changed.

Above, it has already been shown that albedo affects the position of the CF (e.g., Shirley et al. 2018; Kumari et al. 2020). In particular, investigating anorthosite, augite, and forsterite, Shirley et al. (2018) observed a mineral-dependent shift of the CF position to shorter wavelengths with increasing albedo. Compared to ambient conditions, the CF shifts are strongest for anorthite, less strong for forsterite, and weakest for augite (Shirley et al. 2018).

In summary, results from Diviner and laboratory studies underline the complexities of thermal IR spectroscopy and warrant comprehensive preparatory studies and the generation of dedicated spectral data bases in order to enable an accurate interpretation of IR spectra returned from space missions (e.g., Lucey et al. 2017; Bramble et al. 2019).

## 3.3 Laboratory Studies

MERTIS operates in the TIR range, which is uniquely suited to investigate the composition of the hermean surface because in spectral measurements in the 7–14 μm range, rock-forming silicates such as pyroxenes, olivines, and feldspars can be easily detected and characterized by their diagnostic Christiansen features (CF), Reststrahlen bands (RBs), and the Transparency features (TF) (e.g., Salisbury and Wald 1992; Thompson and Salisbury 1993). At wavelengths longer than 7 μm, spectral signatures in silicates stem from characteristic fundamental Si-O vibrations. Thus, FeO- and $TiO_2$-free silicates (e.g., feldspars, Fe-free pyroxenes, and Fe-free olivines) undetectable in the VIS-NIR region, can be detected. Although the positions and shapes of RBs are diagnostic for each mineral, their shapes are affected by crystal orientation as well as grain size. For example, the spectral contrast increases with increasing grain sizes and for grain sizes $<25$ μm, volume scattering is significant. As a result, the spectral contrast decreases within the RBs and a separate emission minimum occurs at about 11.5 μm (870 $cm^{-1}$). This TF, an emissivity minimum (or reflectance maximum), is highly diagnostic for the bulk composition (e.g., Salisbury 1993). In addition, the TF is also highly diagnostic for grain sizes smaller than 25 μm, allowing the determination of grain sizes in the observed regolith. The unambiguous identification of the CF requires an instrument capable of measuring down to a wavelength of 7 μm in order to accurately describe the steep onset between 7 μm and 7.75 μm. Because Cooper et al. (2002) found a significant shift of the position of the CF of solid samples and powders, the physical properties of the hermean surface have to be understood for an accurate interpretation of MERTIS thermal infrared spectra. Similarly, high temperatures (i.e., 420 °C) on Mercury's surface modify the olivine spectrum, shifting the wavelength position of its emissivity features to mimic the spectrum of an olivine strongly enriched in iron (Helbert et al. 2013b). This temperature-dependent spectral behavior indicates that spectroscopic investigations of the surface of Mercury must take into account the local solar time dependency to properly infer the compositions of planetary materials by remote sensing acquisition of future space missions. Comparable studies on pyroxenes show how their absorption bands are more or less dependent on surface temperature on Mercury (Ferrari et al. 2014). Thermal expansion affects the $\sim$7–14 μm (1400–700 $cm^{-1}$) spectral range, defining which diagnostic absorptions are more prominent (Ferrari et al. 2020). In this paper we showed how two minerals

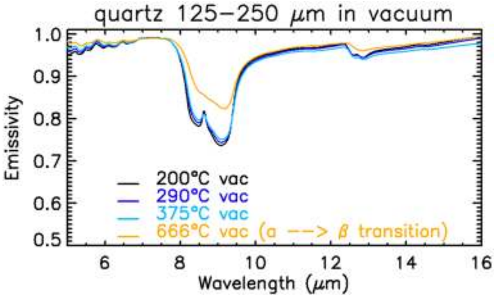

**Fig. 11** Emissivity spectra of a quartz sample taken in vacuum at increasing temperatures

with different thermal expansion coefficients, contained in the same sample, combine in the resulting emissivity spectrum.

The scientific topics outlined in Chap. 3.1 provide the framework for our laboratory studies that we are performing in preparation for the science acquisition phase of MERTIS. To accurately interpret MERTIS remote sensing data, comprehensive laboratory studies on analog materials under simulated environmental conditions of the planet surface are required. These spectral studies are complemented with thermal and spectral modeling as well as telescopic observations.

### *3.3.1 Laboratories*

The MERTIS team is operating two complementary spectral laboratories, i.e., the Planetary Spectroscopy Laboratory (PSL) in Berlin and Infrared and Raman for Interplanetary Spectroscopy (IRIS) laboratory in Münster, following common standards. For example, both laboratories measure samples at grain sizes of 0–25 μm, 25–63 μm, 63–125 μm, and 125–250 μm. Both laboratories are equipped with thermal chambers that allow spectral measurements under vacuum conditions and at Mercury-relevant temperatures of up to 500 °C. Detailed description of the PSL facility can be found in Maturilli et al. (2006, 2008), Helbert and Maturilli (2008), Varatharajan et al. (2019a), and Morlok et al. (2016a, 2016b, 2017a, 2017b, 2017c, 2019, 2020a, 2020b, 2020c) for IRIS.

At the PSL we are measuring the emissivity of planetary analog materials in the spectral range from 1 μm to 50 μm, in vacuum and under simulated Mercury daytime surface temperatures (100 °C to 500 °C). Figure 11 shows an example of emissivity measurements taken in vacuum for a quartz sample (125–250 μm grain size range) at various temperatures. The emissivity spectrum taken at 666 °C surface temperature shows the spectral effects of the $\alpha$- to $\beta$-transition typical for the tetrahedral molecule of quartz (a continuous framework of $SiO_4$). In fact, the room-temperature form of quartz, trigonal $\alpha$-quartz, undergoes a reversible transformation in the crystal structure at 573 °C to form hexagonal $\beta$-quartz, which is accompanied with a volume change (Deer et al. 1966).

Emissivity measurements are recorded using an external emissivity chamber (designed at DLR), attached to a Bruker Vertex80V FTIR spectrometer with a nitrogen-cooled MCT detector and a KBr beamsplitter. Several Mercury analogs have been measured in this configuration to determine their emissivity behavior under simulated daytime surface conditions of Mercury, including silicates (Maturilli et al. 2014; Maturilli et al. 2017; Varatharajan et al. 2020; Ferrari et al. 2014, 2020), sulfides (Varatharajan et al. 2019a, 2019b; Helbert et al. 2013b; Carli et al. 2019), and graphite (Maturilli et al. 2019). A unique spectral library is being created for the spectral range of 7–14 μm, at five temperatures (100, 200, 300, 400, 500 °C) and in a low vacuum environment, to support MERTIS observations. During the emissivity measurements, the temperature is increased gradually up to the chosen values and is controlled by means of temperature sensors located inside the chamber, in contact with the surface of the sample, and the sample cup rim. Along with emissivity studies, reflectance spectra of both fresh (before heating) and thermally processed (500 °C) analogues are studied at varying phase angles (26–80°) across the ultraviolet (UV) to far-infrared (FIR) spectral range covering 0.2–100 µm (Maturilli et al. 2016a). During the emissivity measurements, the analogs are continuously monitored using a webcam. This allows us to study the chemical, physical, and morphological weathering of fresh analogs while they undergo extreme thermal weathering conditions during measurements. The influence of emerging angle on laboratory emissivity data was quantified in Maturilli et al. (2016b). An FTIR microscope Bruker HYPERION 2000 is in use at PSL to allow microscopic analyses in transmission and reflectance in the VIS/VNIR/MIR spectral ranges.

At the IRIS laboratory, we are measuring reflectance in the spectral range from 2 µm to 18 µm. An external Harrick Emission Cell is in the process of being commissioned. This extension will allow the complementary study of our samples in emission.

Bulk powder analyses are made with a Bruker Vertex 70v infrared system, using a cooled MCT detector. An additional Bruker 80v system was installed for further studies in the UV/VIS-NIR range. Because thermal conduction of the atmosphere in the pore space might reduce the thermal gradient (Henderson and Jakosky 1994, 1997; Sprague et al. 1994), all studies are done in vacuum and under controlled thermal conditions. In order to simulate the effects of varying grain sizes in the 2–18 µm wavelength range, spectra were made of powdered size fractions of bulk material (0–25 µm, 25–63 µm, 63–125 µm, and 125–250 µm).

In order to emulate various orbital geometries, bulk powders are analyzed using a Bruker A513 variable mirror stage. Geometries used are 20° incidence ($i$) and 30° emergence, $i = 30°$ and $e = 30°$, as well as $i = 13°$ and $e = 13°$ (Weber et al. 2020a). Micro-FTIR studies are done either with a Bruker Hyperion 2000 IR microscope at the Hochschule Emden/Leer, a Bruker Hyperion 3000 equipped with a focal plane array (FPA) mapping detector at the University of Bern or a Perkin Elmer Spotlight 400 FTIR FPA Imaging System at the University of Manchester. These micro-FTIR spectra are obtained of polished thin sections if only small amounts of materials are available, or to investigate the spectral features of different components in mixtures. All samples undergo a detailed physical and chemical characterization before the infrared studies. This includes optical microscopy, scanning electron microscopy (SEM), Raman spectroscopy, and electron microprobe (EMPA) analyses.

In addition, SW is greatly affecting the hermean spectra. Thus, in order to understand these effects, we are performing comprehensive investigations using IR and UV lasers, ion radiation, and shock experiments to simulate SW effects.

Because TIR spectra are sensitive to temperature, we need to understand the thermal behavior of the hermean surface with its large temperature variations each diurnal period. As a result of the highly eccentric orbit and the 3:2 spin orbit resonance, the insolation and resulting temperatures vary at different latitudes and longitudes. Due to the lack of an atmosphere, surface temperatures rapidly change at sunrise and sunset between less than 100 K and up to 700 K at 0° W and 180° W longitudes, and up to 570 K at 90° W and 270° W longitudes, which results in hot and warm poles at the equator (Fig. 12). To better understand these temperatures, we developed a thermal model for the surface of Mercury.

### 3.4 Building a Thermal IR Data Base

In preparation of the expected surface spectra from MERTIS, we created the Berlin Emissivity Database (BED) (Maturilli et al. 2008, 2014) and the Infrared and Raman for Inter-

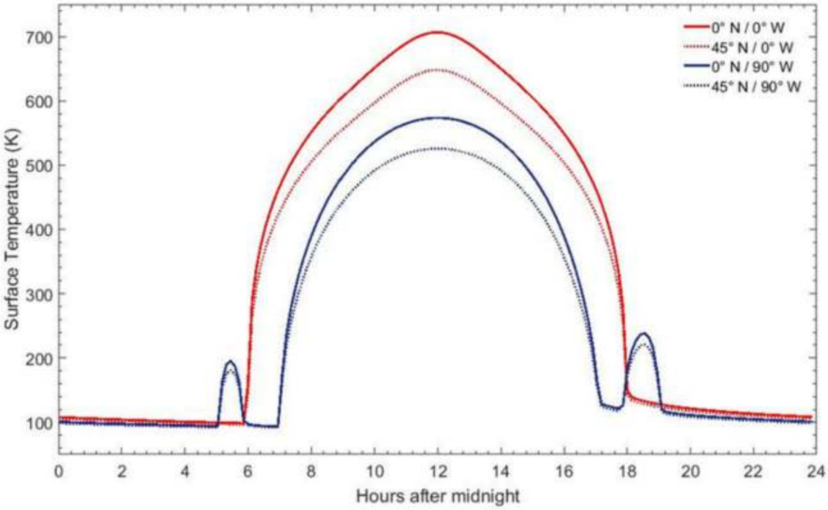

**Fig. 12** Surface temperatures as a function of local time at different locations. Results at the equator are plotted as solid lines, the dotted lines represent latitudes 45° N. Red color indicates temperatures at 0° N longitude ("hot pole" (Morrison 1970)), while blue indicates longitude 90° W ("warm pole" (Morrison 1970)). Results for longitudes 0° W and 90° W equal longitudes 180° W and 270° W, respectively. During perihelion, Mercury's orbital velocity exceeds its spin rate, which results in a secondary sunrise and sunset at 90° longitudes

planetary Spectroscopy (IRIS) spectral database (Weber et al. 2018). Both libraries contain spectral measurements of numerous planetary analog materials as well as results from our sample characterization (e.g., optical microscopy, VIS/IR-microscopy, EMPA, SEM/EDX, Raman).

Our studies of analog materials for the MERTIS-TIR database cover both natural and synthetic materials. Natural rock and mineral samples provide 'ground truth', being materials that actually formed in natural environments (especially in the case of meteorites). However, they are frequently of limited use, since they tend to include impurities or contamination. Furthermore, it is often difficult to find the 'right' natural analogs that fit directly into the compositional range needed for our studies. So, the wealth of chemical data now available from the MESSENGER mission allows us to synthesize materials compositionally similar to the expected surface rocks.

Another step is to combine all these data and compare them with remote sensing data by data-deconvolution (Rommel et al. 2017; Grumpe et al. 2018). Our first list of Mercury analogs dates back more than 10 years (Helbert et al. 2007). Comparison with the information about Mercury's surface gained from the MESSENGER mission confirms that our list is still containing the most accepted surface analogs for the planet.

## 3.5 Selected Scientific Results

In the following sub-chapters, we will present some results of our laboratory program. We will focus on results on analog materials with MESSENGER-derived compositions, impact rocks and glasses, meteorites, lunar samples, space weathering, thermal modeling, ab initio thermal modeling of emissivity spectra, data deconvolution, and telescopic observations.

### *3.5.1 Analogs*

In the absence of hermean meteorites, we performed a number of investigations on analog materials, both natural and synthetic. The compositions of our synthetic analogs were based on the chemistry of distinct hermean surface areas identified by the MESSENGER mission (Vander Kaaden et al. 2017; Namur and Charlier 2017; Morlok et al. 2017b, 2019). In particular, we investigated the results from crystallization experiments on magmas with hermean compositions and under reducing conditions expected for Mercury (Namur and Charlier 2017), which represent major terranes namely the low-Mg Northern Volcanic Plains (NP-LMg), high-Mg Northern Volcanic Plains (NP-HMg), Intercrater Terrane (ICT), High-Mg Province (HMR), and Smooth Plains (SP) of Mercury (Varatharajan et al. 2018a, 2018b). These samples are 5 × 5 $\text{mm}^2$ in area, containing major minerals including forsterite, diopside, enstatite, plagioclase, and locally FeSi. The experimental products are among the most unique Mercury surface analog samples and were either studied directly with bi-directional and nano-FTIR spectroscopy to characterize their spectral behavior in the MERTIS spectral range, or served as basis for analogs synthesized for Mercury's regolith, surface, and mantle (Varatharajan et al. 2018b; Morlok et al. 2017b, 2019).

**Synthetic Glasses** For the analogs, we first focused on glasses, which formed from whole rock melting because of impacts, volcanism, and SW and, thus, are expected to form an important part of the surface regolith. The synthetic glasses for Mercury's surface regions and regolith made under different oxidation states display mostly spectra typical for amorphous materials with a dominating, single RB at 9.5–10.7 µm, a CF at 7.9–8.3 µm, and a TF at 11.8–12.2 µm (Morlok et al. 2017b, 2019).

Up to now, we measured six bulk silicate Mercury analogs, which exhibit varying CF positions from 8.1 to 9 µm, with RB crystalline features of various olivines dominating in most samples. Dendritic crystallization starts at a MgO content higher than 23wt.% MgO, resulting in RB features of forsterite (Morlok et al. 2017b, 2019).

In addition to the natural impact rocks, synthetic glass formed in laboratory impact experiments under controlled conditions can be investigated to simulate the effects of high-velocity impacts. In a first study, we used run products from pulsed laser experiments on basaltic rocks in collaboration with the Museum für Naturkunde, Berlin (Hamann et al. 2016; Morlok et al. 2020a). These laser impact experiments on basalts produced pure glass materials forming in the target basalt, with CFs at 8.8–8.9 µm, strong RBs at 10.3–10.5 µm, and only weak TFs. Both, spectral features and chemical composition of the glass, indicate that evaporation of target material took place (Hamann et al. 2016; Morlok et al. 2020a).

We carried out another study in which two series of silicate glasses were synthesized from natural samples in order to characterize their near- and mid-IR spectra (Pisello et al. 2018). In reflectance measurements, we observed the shift of the CF to be linearly correlated with the $SiO_2$ content, whereas for emissivity measurements the same dependency was observed with temperature.

Another crucial Mercury surface analog are feldspars (Helbert et al. 2007; Sprague et al. 2009; Reitze et al. 2020). Due to their intrinsic spectral complexity, detailed studies of the complete crystallographic and compositional range are necessary. Our investigations of the Na- and K-rich alkali feldspars showed that the autocorrelation method allows differentiating between the compositional and the order/disorder influences seen in the powder reflectance spectra in the wavelength range between 7 µm to 14 µm (Reitze et al. 2020). In particular, decreasing the degree of order led to broader RBs and a feature shift. In addition, applying the autocorrelation method we were able to determine the Or content of feldspar at different grain sizes (Reitze et al. 2020).

**Igneous Rocks** The hermean igneous silicate rocks are Mg-richer and Al-, Ca- and Fe-poorer than those of the Moon and Earth, and are enriched in volatiles and alkali elements (e.g., Nittler et al. 2018, and references therein). In particular, the unexpected presence of S suggests the presence of sulfides associated with high concentration of Ca and Mg (Nittler et al. 2018, and references therein). VIS-MIR (Visible-Mid Infrared) and TIR (Thermal Infrared) emissivity and reflectance spectra of mixtures composed of a Mg-rich silicate and a sulfide component were conducted at PSL under simulated Mercury surface conditions to understand the evolution of the spectral and physical behavior of these sulfides under extreme temperature conditions (Varatharajan et al. 2019a). The study showed that major sulfides such as CaS, MgS, and NaS can be unambiguously identified in the TIR region and, thus, indicate the possibility for detecting them with MERTIS. Hence, MERTIS will enable the mineralogic mapping of volatile-rich deposits on Mercury's surface. Our preliminary results also document temperature effects on the emissivity spectra at four different temperatures. In addition, it is evident that the CF and RBs are influenced in different ways by the relative abundance of sulfides/silicates. Reflectance spectra show variations in the VNIR with a reddening and a weakening of absorptions after heating (Carli et al. 2019).

In order to detect and map the silicate mineralogy of Mercury with MERTIS, the emissivity behavior of a wide range of fine powdered silicates ($<25$ μm) has been studied in vacuum at temperatures from 100 °C to 500 °C (100 °C steps) (Varatharajan et al. 2020). The studied silicates include a) olivine: forsterite ($Fo_{89}$), b) pyroxenes: enstatite, diopside, c) plagioclase feldspar: hypersthene, anorthite, labradorite, andesine, oligoclase, d) potassium feldspar: orthoclase, and e) feldspathoid: nepheline. The emissivity of these silicates (at grain size of $<25$ μm) at 7–14 μm as a function of temperature under vacuum conditions will be incorporated into the spectral library for the MERTIS data analyses and MIR telescope data analyses of Mercury (Varatharajan et al. 2020).

**Impact Rocks** In addition to synthetic and experimental studies, we looked at complementary natural impact rocks. Studies of terrestrial impactites can provide estimates of the effects of shock metamorphism on the mid-infrared spectral properties of planetary materials.

We analyzed in detail samples from the Nördlinger Ries crater in Southern Germany (Morlok et al. 2016a), and 14 impact melt glass samples and tektites from various terrestrial craters (Morlok et al. 2016b), covering the compositional range from highly felsic to mafic/basaltic.

Nördlinger Ries impact melt glass and suevite have spectra dominated by RBs at 9.3–9.6 μm. (Morlok et al. 2016a) (Fig. 1b). Among other studied melt rocks, the characteristic CF is located between 7.3 μm (Libyan Desert Glass) and 8.2 μm (Dellen). Most samples show mid-infrared spectra typical of highly amorphous material, dominated by a strong RB between 8.9 μm (Libyan Desert Glass) and 10.3 μm (Dellen) (Morlok et al. 2016b).

**Meteorites and Lunar Samples** *NWA 7325* Another focus are potential meteorites from Mercury such as Northwest Africa (NWA) 7325 (Irving et al. 2013) and aubrites. For the understanding of the surface composition and mineralogy of Mercury, we performed a comprehensive investigation of the unique achondrite NWA 7325 (Weber et al. 2016; Helbert et al. 2013c) and of various lithologies in two aubrites (Peña Blanca Spring and Norton County, Morlok et al. 2020b). The NWA 7325 sample was investigated in a consortium study by Weber et al. (2016). As a result, we can exclude an origin of NWA 7325 from Mercury, because the analyses show isotopic and chemical similarities to achondrites. In addition, infrared spectroscopy indicates that a direct relationship between NWA 7325 and planet Mercury can be ruled out (Helbert et al. 2013c; Weber et al. 2016).

*Lunar Meteorites* The lunar regolith is another group of planetary materials of interest, given the similarities like originating from surfaces of atmosphere-less bodies. For the lunar meteorites, one of the aims is to connect the surface processes of regolith formation (like impacts) with spectral features. In collaboration with the University of Manchester, we studied both lunar meteorites and Apollo samples. For example, the physical state of feldspathic phases that have been subject to varying levels of shock in the grouped lunar meteorites Miller Range 090034, 090070, and 090075 were investigated (Martin et al. 2017). Emissivity and reflectance of the Apollo 16 lunar highlands sample 62231.44 are contained in the BED spectral library (Maturilli et al. 2008; Maturilli and Helbert 2014). On the basis of a specific infrared wavelength band ratio (9.40/10.73 µm), the origin and shock history of a series of lunar meteorites (MIL 090034, MIL 090070, and MIL 090075) with highly shocked feldspathic phases being related to events in its geological evolution were determined (Martin et al. 2017).

*Other Meteorites* In addition, further meteorites were investigated to augment the database: Carbonaceous chondrites (Morlok et al. 2020c) as well as ordinary chondrites (LL6) Stubenberg (Bischoff et al. 2017) and Renchen (L5-6) (Bischoff et al. 2019), both recent falls that provide fresh material for investigations. Ordinary chondrites Stubenberg (LL6) and Renchen (L5-6) provided spectral data of very common meteorite matter in the Solar System, thus allowing to distinguish potential contamination of regolith with impact material. In order to determine the controls on the reflectance spectra of hydrated and dehydrated carbonaceous chondrites, reflectance spectra were measured for a series of samples with well-determined mineralogy, water content, and thermal history (Beck et al. 2018). A thin section of a weathered meteorite (enstatite chondrite) has been investigated and classified using a FTIR microscope and spectral differences associated with different degrees of weathering could be noticed and quantified.

The Chelyabinsk meteorite contains several lithologies with increasing influence of impact shock from 'pristine' ordinary chondrite material (LL6) to the shock-darkened lithology and the impact melt lithology as endmembers. We investigated the Chelyabinsk meteorite, in order to investigate the influence of increasing impact shock on FTIR spectra in a natural sample. Having been collected immediately after its observed fall, it provides fresh, unaltered material containing various lithologies that underwent impact/collision shock (Morlok et al. 2017a; Kaeter et al. 2018). We observe the fading/disappearing of spectral features with increasing degrees of shock. Most prominent is the loss of features between 10.8 and 11.3 µm (Morlok et al. 2017a).

### 3.5.2 *Space Weathering*

Space weathering (SW) processes on planetary surfaces of all atmosphereless bodies are caused by solar flares, high particle fluxes, impacts with various sized impactors, and microparticle flux. These processes affect the surface by forming and gardening of a regolith layer as well as the formation of nanophase Fe metal ($npFe^0$) (e.g., Hapke 2001; Wiesli et al. 2003; Domingue et al. 2014).

Considering the atmosphereless bodies were exposed to these SW effects for an extended time period, large changes in terms of petrography and surface chemical evolution are expected (e.g., Chapman 2004). Thus, it is reasonable to assume that spectra in the visible and infrared wavelength ranges (near- and mid-infrared) obtained via remote sensing show significant alteration features.

To study SW processes and their effects on thermal IR spectra, we simulated micrometeorite bombardment as one possible source of SW. Our results from experiments on a partly bombarded surface with a pulsed intense infrared laser, generating ∼15 mJ per pulse in high vacuum, confirmed that in the VIS/NIR spectral range, space weathering results in a darkening, reddening, and a decrease in the depths of absorption bands (e.g., Noble et al. 2001; Noble and Pieters 2003; Pieters et al. 1993, 2000; Weber et al. 2020b). In the MIR spectral range, space weathering results in an increase of the TF because of gardening from micrometeorite bombardment of the pressed mineral powder. Besides gardening, space weathering also results in significant difference in the microstructure of the affected minerals. Our TEM studies revealed that space-weathered layers in olivine and pyroxene differ in their respective thickness, ∼450 nm in olivine, 100–250 nm in pyroxene, as well as in developed "nanostratigraphy" of laser-ablated material, like nanophase iron (npFe). We found that olivine is more rapidly space weathered than pyroxene (Weber et al. 2020b). However, this finding is inconsistent with TEM investigations of Keller et al. (2016) who found that pyroxene samples from asteroid Itokawa are more rapidly affected by space weathering than olivine. We are now extending our studies to a 193 nm ArF UV excimer laser operating with an energy density of 2.5 J/cm$^2$. Preliminary results of a completely bombarded surface show a visible darkening of the surface combined with the loss of the TF in the MIR spectra, which we interpret as an effect of agglutination (Weber et al. 2019, 2020a).

Furthermore, we continued our studies with a set of new experiments. For example, we performed shock recovery experiments at the Ernst Mach Institute in Freiburg, making use of the gas gun to shock samples to levels of up to 30 GPa. In addition, we are collaborating on simulating SW effects by ion bombardment.

### *3.5.3 Thermal Modeling*

Global surface temperature maps were calculated based on initial data from MESSENGER MDIS albedo and topography data (Hawkins et al. 2007; Becker et al. 2016). Figure 13 shows the map of maximum surface temperatures superposed on the albedo map (Bauch et al. 2020). The total range of temperatures in the covered latitude band is from 450 K to 700 K. Temperatures are highest at the equator at longitudes 0° W and 180° W. Red colors indicate temperatures above 650 K and occur at latitudes $<45°$.

### *3.5.4 Ab Initio Thermal Modelling of Emissivity Spectra*

Data interpretation must take into account changes in spectral characteristics induced by high-temperature conditions during the hermean day. High-temperature mid-IR spectra were modelled by means of Hartree-Fock (HF) and Density Functional Theory (DFT) calculations to predict the changes in spectral features due to the increase of temperature (Stangarone et al. 2017). The approach was first tested by modelling forsterite ($Mg_2SiO_4$). We compared our results with the experimental measurements of a natural olivine ($Fo_{89}$; up to 900 K) carried out at PSL and found that the main changes in spectral characteristics due to temperature were successfully reproduced in the model (Fig. 14). Thus, for relatively simple orthorhombic minerals, the computational approach employed can reliably be used to predict band shifts due to temperature. A particularly good agreement between measurements and simulated data is observed in the spectral range of ∼8–17 µm (1200–600 cm$^{-1}$). The discrepancies between calculated and experimental spectra can largely be explained by the

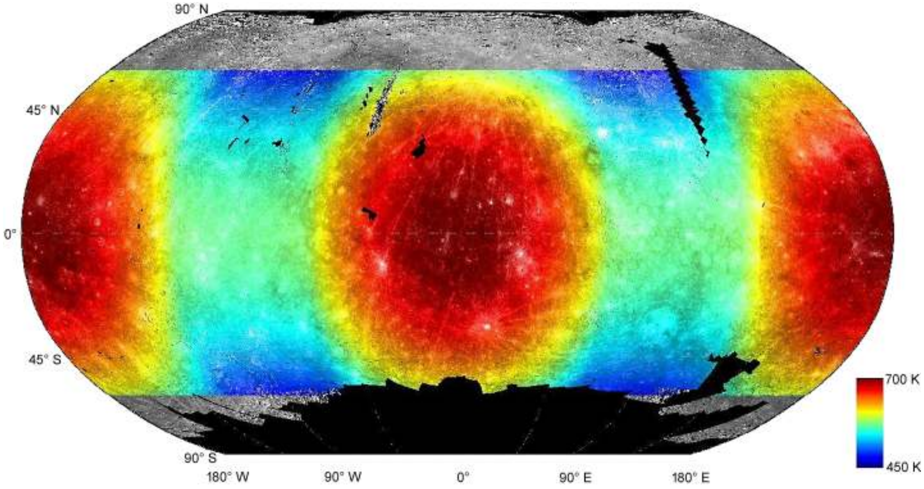

**Fig. 13** Map of local maximum surface temperatures (in K) with a resolution of 16 pixels per degree superposed on the albedo map. Red colors indicate temperatures >600 K, which occur at the hot poles (0° W and 180° W longitudes). Temperatures are lower at higher latitudes, but also at longitudes 90° W and 270° W. Temperature differences due to brightness (e.g., bright crater rays) are also visible

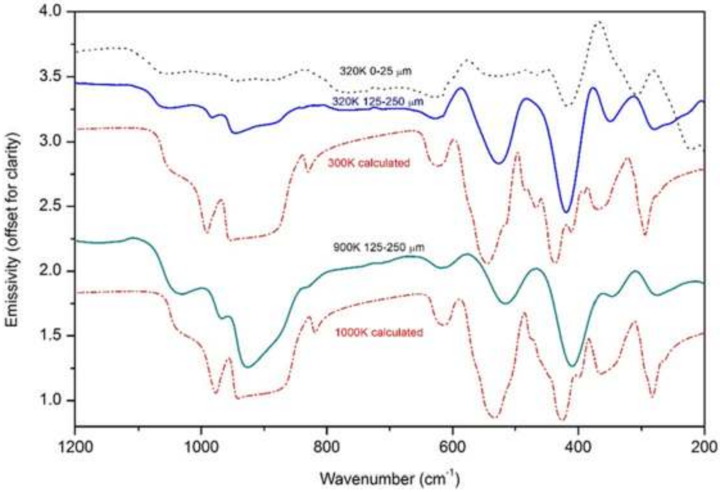

**Fig. 14** Comparison between emissivity mid IR spectra (calculated as 1-R) and experimental emissivity measurements. Solid line: Experimental thermal emissivity spectra of $Fo_{89}$ measured at 320 K and 900 K (extreme situations). Dotted lines: Calculated IR reflectance (inverted) bands of an $Mg_2SiO_4$ ($Fo_{100}$) endmember. Spectra are offset for clarity

fact that with this approach it is not possible to model the band shapes due to grain sizes or potential preferential orientation in a granular sample. In addition, it is known that for some silicates, the spectral features due to the iron content overlap with the effects of temperature (Helbert et al. 2013b).

### 3.5.5 Data Deconvolution

Planetary surfaces are composed of a variety of different minerals and grain sizes. Thus, the obtained spectral data are mixtures of these minerals and a non-linear deconvolution of the spectral data is necessary to quantify mineral abundances (Poulet and Erard 2004). First results with binary pyroxene and olivine mixtures show that it is possible to calculate the starting mixtures within a 3% deviation (Bauch et al. 2019, 2020; Weber et al. 2019, 2020a).

### 3.5.6 Telescope Observations

On December 16–18, 2018, we obtained global disk-resolved NIR spectroscopic data of Mercury at the Infrared Telescope Facility (IRTF) on Mauna Kea, HI, using the SpeX 0.7–5.3 μm Medium-Resolution Spectrograph and Imager. During these observations, Mercury was ∼63–70% illuminated. We observed geochemical terrains, including NVP-LMg and NVP-HMg volcanic plains, and intermediate terrain (IT) in the spectral region spanning 0.6–4.2 μm. These observations yielded new information of the surface mineralogy of different geochemical terrains on Mercury and also help improving our preparations and planning of our MERTIS data acquisition and science (Varatharajan et al. 2019b).

For 2020, we are planning new telescopic observations to observe the Mercurian day- and nightside in the mid-infrared from 7–14 μm microns using the MIRSI (Mid-Infrared Imager and Spectrometer) instrument for the same geochemical terranes observed during 2018 (Varatharajan et al. 2018a). These telescopic spectroscopic observations of Mercury across a wide wavelength range (0.7–14 μm) along with spectral unmixing using our spectral library will give us deeper understanding of surface composition of various geochemical regions on Mercury.

## 4 Conclusions

The Mercury Radiometer and Thermal Infrared Spectrometer (MERTIS) is an innovative miniaturized spectrometer that explores a wavelength region of the electromagnetic spectrum that has never been utilized before for the investigation of the mineralogy and composition of the hermean surface. The instrument combines a push-broom TIR imaging spectrometer in the range from 7–14 μm and a thermal radiometer (7–40 μm) to investigate the composition, temperature, thermal inertia, and texture of Mercury's surface.

Investigation of the compositional and physical properties of Mercury's surface with MERTIS, in concert with other instruments, will allow us to make significant progress in understanding the origin of the planet, its core formation, and its geologic/thermal history and evolution.

The instrument fulfils all requirements (e.g., mass, power, performance) and is fully operational onboard the BepiColombo spacecraft. In preparation of the data acquisition at Mercury, we developed an innovative operations plan to maximize the scientific output while at the same time saving spacecraft resources (e.g., data downlink). We will use the upcoming fly-bys to further test and adapt our software and operational procedures. In parallel, we are running a comprehensive suite of spectroscopic measurements in our laboratories on relevant analog materials, perform extensive spectral modeling, examine space weathering effects, and model the thermal behavior of the hermean surface. In conclusion, the MERTIS team is undertaking action at multiple levels to be prepared for Mercury.

**Acknowledgements** We gratefully acknowledge the superb work of the MERTIS design, engineering, and science team. This work was supported by DLR grant 50 QW 1302/1701 in the framework of the BepiColombo mission. The MERTIS Science Team consists of following persons: G. Arnold, M. Banaszkiewicz, K. Bauch, J. Benkhoff, A. Bischoff, M. Blecka, N. Bowles, S. Calcutt, L. Colangeli, M. D'Amore, S. Erard, S. Fonti, B. T., Greenhagen, O. Groussain, J. Helbert, H. Hiesinger, H. Hirsch, J. Jahn, R. Killen, J. Knollenberg, E. Kührt, E. Lorenz, I. Mann, U. Mall, A. Maturilli, A. Morlok, L. Moroz, G. Peter, M. Rataj, M. Robinson, W. Skrbek, T. Spohn, A. Sprague, D. Stöffler, A. Stojic, F. Taylor, I. Varatharajan, H. Venus, J. Warrell, I. Walter, I. Weber, A. Witzke, C. Wöhler.

**Author Contribution** All listed authors contributed significantly to this publication.

**Funding Information** Open Access funding provided by Projekt DEAL. This work was supported by DLR grant 50 QW 1302/1701 in the framework of the BepiColombo mission.

**Conflict of interest** Not applicable.

**Availability of data material** Results described in this instrument paper are available in individual peer-reviewed publications.

**Publisher's Note** Springer Nature remains neutral with regard to jurisdictional claims in published maps and institutional affiliations.

**Open Access** This article is licensed under a Creative Commons Attribution 4.0 International License, which permits use, sharing, adaptation, distribution and reproduction in any medium or format, as long as you give appropriate credit to the original author(s) and the source, provide a link to the Creative Commons licence, and indicate if changes were made. The images or other third party material in this article are included in the article's Creative Commons licence, unless indicated otherwise in a credit line to the material. If material is not included in the article's Creative Commons licence and your intended use is not permitted by statutory regulation or exceeds the permitted use, you will need to obtain permission directly from the copyright holder. To view a copy of this licence, visit http://creativecommons.org/licenses/by/4.0/.

## References

J.B. Adams, T.B. McCord, C.M. Pieters, C.R. Chapman, A.E. Metzger, T.V. Johnson, I. Adler, M.J. Bielefeld, Remote sensing of basalts in the solar system, in *Basaltic Volcanism Study Project (BVSP), Basaltic Volcanism on the Terrestrial Planets*, ed. by T.R. McGetchin, R.O. Pepin, R.J. Phillips (Pergamon, New York, 1981), pp. 439–490

G.E. Arnold, H. Hiesinger, J. Helbert, G. Peter, I. Walter, MERTIS-thermal infrared imaging of Mercury: advances in mid-IR remote sensing technology for planetary exploration, in *SPIE Infrared Rem. Sens. Instr.*, vol. 7808, p. 780801 (2010). https://doi.org/10.1117/12.860144

K.E. Bauch, H. Hiesinger, A. Morlok, M.P. Reitze, I. Weber, M. Tiedecken, J. Helbert, Deconvolution of laboratory IR spectral reflectance data for MERTIS onboard the ESA/JAXA BepiColombo mission. Lunar Planet. Sci. **50**, 2521 (2019)

K.E. Bauch, H. Hiesinger, B.T. Greenhagen, J. Helbert, Estimation of surface temperatures on Mercury in preparation of the MERTIS experiment onboard BepiColombo. Icarus (2020). https://doi.org/10.1016/j.icarus.2020.114083, in press

P. Beck, A. Maturilli, A. Garenne, P. Vernazza, J. Helbert, E. Quirico, B. Schmitt, What is controlling the reflectance spectra (0.35–150 μm) of hydrated (and dehydrated) carbonaceous chondrites? Icarus **313**, 124–138 (2018). https://doi.org/10.1016/j.icarus.2018.05.010

K.J. Becker, M.S. Robinson, T.L. Becker, L.A. Weller, K.L. Edmundson, G.A. Neumann, M.E. Perry, S.C. Solomon, First global digital elevation model of Mercury. Lunar Planet. Sci. **47**, 2959 (2016)

C.J. Bennett, J.L. McLain, M. Sarantos, R.D. Gann, A. DeSimone, T.M. Orlando, Investigating potential sources of Mercury's exospheric calcium: photon-stimulated desorption of calcium sulfide. J. Geophys. Res. **121**, 137–146 (2016). https://doi.org/10.1002/2015JE004966

W. Benz, W.L. Slattery, A.G.W. Cameron, Collisional stripping of Mercury's mantle. Icarus **74**, 516–528 (1988)

W. Benz, A. Anic, J. Horner, J.A. Whitby, The origin of Mercury. Space Sci. Rev. **132**, 189–202 (2007)

A. Bischoff, J.-A. Barrat, K. Bauer, C. Burkhardt, H. Busemann, S. Ebert, M. Gonsior, J. Hakenmüller, J. Halofa, D. Harries, D. Heinlein, H. Hiesinger, R. Hochleitner, V. Hoffmann, M. Kaliwoda, M. Laubenstein, C. Maden, M.M.M. Meier, A. Morlok, A. Pack, A. Ruf, P. Schmitt-Kopplin, M. Schönbächler, R.C.J. Steele, P. Spurny, K. Wimmer, The Stubenberg meteorite – an LL6 chondrite fragmental breccia recovered soon after precise prediction of the strewn field. Meteorit. Planet. Sci. **52**, 1683–1703 (2017). https://doi.org/10.1111/maps.12883

A. Bischoff, J.-A. Barrat, J. Berndt, J. Borovicka, C. Burkhard, H. Busemann, J. Hakenmüller, D. Heinlein, J. Hertzog, J. Kaiser, C. Maden, M.M.M. Meier, P. Morino, A. Pack, M. Patzeck, M.P. Reitze, M. Rüfenacht, P. Schmitt-Kopplin, M. Schönbächler, P. Spurny, I. Weber, K. Wimmer, T. Zikmund, The Renchen L5-6 chondrite breccia—the first confirmed meteorite fall from Baden-Württemberg (Germany). Geochemistry **79**, 125525 (2019). https://doi.org/10.1016/j.chemer.2019.07.007

D.T. Blewett, P.G. Lucey, B.R. Hawke, G.G. Ling, M.S. Robinson, A comparison of mercurian reflectance and spectral quantities with those of the Moon. Icarus **129**, 217–231 (1997)

D.T. Blewett, B.R. Hawke, P.G. Lucey, Lunar pure anorthosite as a spectral analog for Mercury. Meteorit. Planet. Sci. **37**, 1245–1254 (2002)

D.T. Blewett, M.S. Robinson, B.W. Denevi, J.J. Gillis-Davis, J.W. Head, S.C. Solomon, G.M. Holsclaw, W.E. McClintock, Multispectral images of Mercury from the first MESSENGER flyby: analysis of global and regional color trends. Earth Planet. Sci. Lett. **285**, 272–282 (2009)

D.T. Blewett, B.W. Denevi, M.S. Robinson, C.M. Ernst, M.E. Purucker, S.C. Solomon, The apparent lack of lunar-like swirls on Mercury: implications for the formation of lunar swirls and for the agent of space weathering. Icarus **209**, 239–246 (2010). https://doi.org/10.1016/j.icarus.2010.03.008

D.T. Blewett, C.M. Ernst, S.L. Murchie, F. Vilas, Mercury's hollows, in *Mercury - The View After MESSENGER*, ed. by S.C. Solomon, L.R. Nittler, B.J. Anderson (Cambridge University Press, Cambridge, 2011a), pp. 324–345

D.T. Blewett, N.L. Chabot, B.W. Denevi, C.M. Ernst, J.W. Head, N.R. Izenberg, S.L. Murchie, S.C. Solomon, L.R. Nittler, T.J. McCoy, Z. Xiao, D.M. Baker, C.I. Fassett, S.E. Braden, J. Oberst, F. Scholten, F. Preusker, D.M. Hurwitz, Hollows on Mercury: MESSENGER evidence for geologically recent volatile-related activity. Science **333**, 1856–1859 (2011b)

D.T. Blewett, N.L. Chabot, B.W. Denevi, C.M. Ernst, The nature of Mercury's hollows, and space weathering close to the Sun, in *Mercury: Current and Future Science of the Innermost Planet. LPI Contrib. 2047* (2018), p. 6051

M.S. Bramble, Y. Yang, W.R. Patterson, R.E. Milliken, J.F. Mustard, K.L. Donaldson Hanna, Radiometric calibration of thermal emission data from the Asteroid and Lunar Environment Chamber (ALEC). Rev. Sci. Instrum. **90**, 093101 (2019). https://doi.org/10.1063/1.5096363

S.M. Brown, L. Elkins-Tanton, Compositions of Mercury's earliest crust from magma ocean models. Earth Planet. Sci. Lett. **286**, 446 (2009)

T.H. Burbine, T.J. McCoy, L.R. Nittler, G.K. Benedix, E.A. Cloutis, Spectra of extremely reduced assemblages: implications for Mercury. Meteorit. Planet. Sci. **37**, 1233–1244 (2002)

B.J. Butler, D.O. Muhleman, M.A. Slade, Mercury - full-disk radar images and the detection and stability of ice at the North Pole. J. Geophys. Res. **98**, 15003–15023 (1993)

P.K. Byrne, J.L. Whitten, C. Klimczak, F.M. McCubbin, L.R. Ostrach, in *Mercury - The View After MESSENGER*, ed. by S.C. Solomon, L.R. Nittler, B.J. Anderson (Cambridge University Press, Cambridge, 2018), pp. 287–323

A.G.W. Cameron, The partial volatilization of Mercury. Icarus **64**, 285–294 (1985)

A.G.W. Cameron, W. Benz, B. Fegley Jr., W. Slattery, The strange density of Mercury - theoretical considerations, in *Mercury*, ed. by F. Vilas, C.R. Chapman, M.S. Matthews (University of Arizona Press, Tucson, 1988), pp. 692–708

C. Carli, G. Serventi, A. Maturilli, S. Ferrari, M. Sgavetti, A. Secchiari, A. Montanini, J. Helbert, Emissivity and reflectance spectra of sulfide-bearing samples: New constraints for the hermean surface composition, in *Geophysical Research Abstracts*, vol. 21 (2019), EGU2019-8326

C.R. Chapman, Space weathering of asteroid surfaces. Annu. Rev. Earth Planet. Sci. **32**, 539–567 (2004)

U.R. Christensen, A deep dynamo generating Mercury's magnetic field. Nature **444**, 1056–1058 (2006)

U.R. Christensen, J. Aubert, P. Olson, Convection-driven planetary dynamos, in *Convection in Astrophysics, Proc. IAU Symposium*, vol. 239, ed. by F. Kupka, I.W. Roxburgh, K.L. Chan (2006), pp. 188–195

M.J. Cintala, Impact-induced thermal effects in the lunar and mercurian regoliths. J. Geophys. Res. **97**, 947–973 (1992)

P.E. Clark, *Dynamic Planet: Mercury in the Context of Its Environment* (Springer, New York, 2007), 219 pp.

B. Cooper, A. Potter, R. Killen, T. Morgan, Mid infrared spectra of Mercury. J. Geophys. Res. **106**, 32803–32814 (2001)

B. Cooper, J.W. Salisbury, R.M. Killen, A.E. Potter, Mid infrared spectral features of rocks and their powders. J. Geophys. Res. **107** (2002). https://doi.org/10.1029/2000JE001462

M. D'Amore, J. Helbert, A. Maturilli, I. Varatharajan, B. Ulmer, T. Säuberlich, R. Berlin, G. Peter, I. Walter, H. Hiesinger, S. Martinez, I.O.d. Landaluce, M. Casale, *Data Processing of the Mercury Radiometer and Thermal Infrared Imaging Spectrometer (MERTIS) Onboard BepiColombo* (SPIE, Bellingham, 2018). https://doi.org/10.1117/12.2321051

M. D'Amore, J. Helbert, A. Maturilli, I. Varatharajan, B. Ulmer, T. Säuberlich, R. Berlin, G. Peter, H. Hiesinger, G. Arnold, *The Mercury Radiometer and Thermal Infrared Imaging Spectrometer (MERTIS) Onboard BepiColombo: First Inflight Calibration Results* (SPIE, Bellingham, 2019). https://doi.org/10.1117/12.2529089

W.A. Deer, R.A. Howie, J. Zussman, *An Introduction to the Rock Forming Minerals* (Longman, Harlow, 1966), pp. 340–355

B.W. Denevi, C.M. Ernst, L.M. Prockter, M.S. Robinson, in *Mercury - The View After MESSENGER*, ed. by S.C. Solomon, L.R. Nittler, B.J. Anderson (Cambridge University Press, Cambridge, 2018), pp. 144–175

D.L. Domingue, C.R. Chapman, R.M. Killen, T.H. Zurbuchen, J.A. Gilbert, M. Sarantos, M. Benna, J.A. Slavin, D. Schriver, P.M. Travnicek, T.M. Orlando, A.L. Sprague, D.T. Blewett, J.J. Gillis-Davis, W.C. Feldman, D.J. Lawrence, G.C. Ho, D.S. Ebel, L.R. Nittler, F. Villas, C.M. Pieters, S.C. Solomon, C.L. Johnson, R.M. Winslow, J. Helbert, P.N. Peplowski, S.Z. Weider, N. Mouawad, N.R. Izenberg, W.E. McClintock, Mercury's weather-beaten surface: understanding Mercury in the context of lunar and asteroidal space weathering studies. Space Sci. Rev. **181**, 121–214 (2014). https://doi.org/10.1007/s11214-014-0039-5

D. Dzurisin, Mercurian bright patches: evidence for physio-chemical alteration of surface material? Geophys. Res. Lett. **4**, 383–396 (1977)

D.S. Ebel, S.T. Stewart, in *Mercury - The View After MESSENGER*, ed. by S.C. Solomon, L.R. Nittler, B.J. Anderson (Cambridge University Press, Cambridge, 2018), pp. 497–515

J.P. Emery, A.L. Sprague, F.C. Witteborn, J.E. Colwell, R.W.H. Kozlowski, D.H. Wooden, Mercury: thermal modeling and mid-infrared (5-12 μm) observations. Icarus **136**, 104–123 (1998)

L.G. Evans, P.N. Peplowski, E.A. Rhodes, D.J. Lawrence, T.J. McCoy, L.R. Nittler, S.C. Solomon, A.L. Sprague, K.R. Stockstill-Cahill, R.D. Starr, S.Z. Weider, W.V. Boynton, D.K. Hamara, J.O. Goldsten, Major-element abundances on the surface of Mercury: results from the MESSENGER gamma-ray spectrometer. J. Geophys. Res., Planets **117** (2012). https://doi.org/10.1029/2012JE004178

S. Ferrari, F. Nestola, M. Massironi, A. Maturilli, J. Helbert, M. Alvaro, M.C. Domeneghetti, F. Zorzi, In-situ high-temperature emissivity spectra and thermal expansion of C2/c pyroxenes: implications for the surface of Mercury. Am. Mineral. **99**, 786–792 (2014)

S. Ferrari, A. Maturilli, C. Carli, M. D'Amore, J. Helbert, F. Nestola, H. Hiesinger, Thermal Infrared emissivity of felsic-rich to mafic-rich analogues of hot planetary regoliths. Earth Planet. Sci. Lett. **534** (2020). https://doi.org/10.1016/j.epsl.2020.116089

T.D. Glotch, J.L. Bandfield, P.G. Lucey, P.O. Hayne, B.T. Greenhagen, J.A. Arnold, R.R. Ghent, D.A. Paige, Formation of lunar swirls by magnetic field standoff of the solar wind. Nat. Commun. **6**, 6189 (2015)

K.A. Goettel, Present bounds on the bulk composition of Mercury: implications for planetary formation processes, in *Mercury*, ed. by F. Vilas, C.R. Chapman, M.S. Matthews (University of Arizona Press, Tucson, 1988), pp. 613–621

T.A. Goudge, J.W. Head, L. Kerber, D.T. Blewett, B.W. Denevi, D.L. Domingue, J.J. Gillis-Davis, K. Gwinner, J. Helbert, G.M. Holsclaw, N.R. Izenberg, R.L. Klima, W.E. McClintock, S.L. Murchie, G.A. Neumann, D.E. Smith, R.G. Strom, Z. Xiao, M.T. Zuber, S.C. Solomon, Global inventory and characterization of pyroclastic deposits on Mercury: new insights into pyroclastic activity from MESSENGER orbital data. J. Geophys. Res. **119**, 635–658 (2014)

B.T. Greenhagen, P.G. Lucey, M.B. Wyatt, T.D. Glotch, C.C. Allen, J.A. Arnold, J.L. Bandfield, N.E. Bowles, K.L. Donaldson Hanna, P.O. Hayne, E. Song, I.R. Thomas, D.A. Paige, Global silicate mineralogy of the Moon from the Diviner lunar radiometer. Science **329**, 1507–1509 (2010)

A. Grumpe, N. Mengewein, D. Rommel, U. Mall, C. Wöhler, Interpreting spectral unmixing coefficients: from spectral weights to mass fractions. Icarus **299**, 1–14 (2018)

C. Hamann, R. Luther, M. Ebert, L. Hecht, A. Deutsch, K. Wünnemann, S. Schäfer, J. Osterholz, B. Lexow, Correlating laser-generated melts with impact-generated melts: an integrated thermodynamic-petrologic approach. Geophys. Res. Lett. **43**, 10,602–10,610 (2016). https://doi.org/10.1002/2016GL071050

B. Hapke, Space weathering from Mercury to the asteroid belt. J. Geophys. Res. **106**, 10039–10074 (2001)

H. Harder, G. Schubert, Sulfur in Mercury's core? Icarus **151**, 118–122 (2001)

J.K. Harmon, M.A. Slade, Radar mapping of Mercury - full-disk images and polar anomalies. Science **258**, 640–643 (1992)

J.K. Harmon, M.A. Slade, R.A. Velez, A. Crespo, M.J. Dryer, J.M. Johnson, Radar mapping of Mercury's polar anomalies. Nature **369**, 213–215 (1994)

D.L. Harris, Photometry and colorimetry of planets and satellites, in *Planets and Satellites*, vol. 3, ed. by G. Kuiper, B.M. Middlehurst (The University of Chicago Press, Chicago, 1961). 272 pp.

S.E. Hawkins, J.D. Boldt, E.H. Darlington, R. Espiritu, R.E. Gold, B. Gotwols, M.P. Grey, C.D. Hash, J.R. Hayes, S.E. Jaskulek, C.J. Kardian, M.R. Keller, E.R. Malaret, S.L. Murchie, P.K. Murphy, K. Peacock, L.M. Prockter, R.A. Reiter, M.S. Robinson, E.D. Schaefer, R.G. Shelton, R.E. Sterner, H.W. Taylor, T.R. Watters, B.D. Williams, The Mercury dual imaging system on the MESSENGER spacecraft. Space Sci. Rev. **131**, 247–338 (2007)

J.W. Head, C.R. Chapman, D.L. Domingue, S.E. Hawkins, W.E. McClintock, S.L. Murchie, L.M. Prockter, M.S. Robinson, R.G. Strom, T.R. Watters, The geology of Mercury: the view prior to the MESSENGER mission. Space Sci. Rev. **131**, 41–84 (2007)

J. Helbert, A. Maturilli, The heat is on - in the Planetary Emissivity Laboratory (PEL) at DLR Berlin. Lunar Planet. Sci. **39**, 2408 (2008)

J. Helbert, L.V. Moroz, A. Maturilli, A. Bischoff, J. Warell, A. Sprague, E. Palomba, A set of laboratory materials for the MERTIS instrument on the ESA BepiColombo mission to Mercury. Adv. Space Res. **40**, 272–279 (2007)

J. Helbert, A. Maturilli, M. D'Amore, Visible and near-infrared reflectance spectra of thermally processed synthetic sulfides as a potential analog for the hollow forming materials on Mercury. Earth Planet. Sci. Lett. **369–370**, 233–238 (2013a)

J. Helbert, F. Nestola, S. Ferrari, A. Maturilli, M. Massironi, G.J. Redhammer, M.T. Capria, C. Carli, F. Capaccioni, M. Bruno, Olivine thermal emissivity under extreme temperature ranges: implication for Mercury surface. Earth Planet. Sci. Lett. **371–372**, 252–257 (2013b)

J. Helbert, A. Maturilli, M. D'Amore, R.L. Klima, N.R. Izenberg, G.M. Holsclaw, W.E. McClintock, The Northwest Africa 7325 meteorite – a potential spectral analog for Mercury? in *EPSC Abstracts*, vol. 8 (2013c), EPSC2013-422

B.G. Henderson, B.M. Jakosky, Near-surface thermal gradients and their effects on mid-infrared emission spectra of planetary surfaces. J. Geophys. Res. **99**, 19,063–19,073 (1994)

B.G. Henderson, B.M. Jakosky, Near-surface thermal gradients and mid-IR emission spectra: a new model including scattering and application to real data. J. Geophys. Res. **102**, 6567–6580 (1997)

B.G. Henderson, P.G. Lucey, B.M. Jakosky, New laboratory measurements of mid-IR emission spectra of simulated planetary surfaces. J. Geophys. Res. **101**, 14,969–14,975 (1996)

H. Hiesinger, J. Helbert (MERTIS Co-I Team), The Mercury Radiometer and Thermal Infrared Spectrometer (MERTIS) for the BepiColombo mission. Planet. Space Sci. **58**, 144–165 (2010). https://doi.org/10.1016/j.pss.2008.09.019

W.M. Irvine, T. Simon, D.H. Menzel, C. Pikoos, A.T. Young, Multicolor photoelectric photometry of the brighter planets. III. Observations from Boyden Observatory. Astron. J. **73**, 807–828 (1968)

A.J. Irving, S.M. Kuehner, T.E. Bunch, K. Ziegler, G. Chen, C.D.K. Herd, R.M. Conrey, S. Ralew, Ungrouped mafic achondrite Northwest Africa 7325: a reduced, iron-poor cumulate olivine gabbro from a differentiated planetary parent body. Lunar Planet. Sci. **44**, 2164 (2013)

R. Jeanloz, D.L. Mitchell, A.L. Sprague, I. de Pater, Evidence for a basalt-free surface on Mercury and implications for internal heat. Science **268**, 1455–1457 (1995)

C.L. Johnson, R.J. Phillips, M.E. Purucker, B.J. Anderson, P.K. Byrne, B.W. Denevi, J.M. Feinberg, S.A. Hauck, J.W. Head, H. Korth, P.B. James, Low altitude magnetic field measurements by MESSENGER reveal Mercury's ancient crustal field. Science **348**, 892–895 (2015)

D. Kaeter, M.A. Ziemann, U. Böttger, I. Weber, L. Hecht, S.A. Voropaev, A.V. Korochantsev, A. Kocherov, The Chelyabinsk meteorite: new insights from a comprehensive electron microscopy and Raman spectroscopy study with evidence for graphite in olivine of ordinary chondrites. Meteorit. Planet. Sci. **53**, 416–432 (2018)

L.P. Keller, E.L. Berger, R. Christoffersen, S. Zhang, Direct determination of the space weathering in lunar soils and Itokawa regolith from sample analyses. Lunar Planet. Sci. **47**, 2525 (2016)

L. Kerber, J.W. Head, S.C. Solomon, S.L. Murchie, D.T. Blewett, L. Wilson, Explosive volcanic eruptions on Mercury: eruption conditions, magma volatile content, and implications for interior volatile abundances. Earth Planet. Sci. Lett. **285**, 263 (2009)

R.M. Killen, Pathways for energization of Ca in Mercury's exosphere. Icarus **268**, 32–36 (2016)

R.M. Killen, J. Benkhoff, T.H. Morgan, Mercury's polar caps and the generation of an OH exosphere. Icarus **125**, 195–211 (1997)

R.L. Klima, B.W. Denevi, C.M. Ernst, S.L. Murchie, P. Peplowski, Global distribution and spectral properties of low-reflectance material on Mercury. Geophys. Res. Lett. **45**, 2945–2953 (2018)

L. Ksanfomality, J. Harmon, E. Petrova, N. Thomas, I. Veselovsky, J. Warell, Earth-based visible and near-IR imaging of Mercury. Space Sci. Rev. **132**, 351–397 (2007)

N. Kumari, T.D. Glotch, K.A. Shirley, Investigation of variation in Christiansen Feature with albedo on the Moon using the Diviner, $M^3$, and Kaguya datasets. Lunar Planet. Sci. **51**, 1697 (2020)

J.C. Leary, R.F. Conde, G. Dakermanji, C.S. Engelbrecht, C.J. Ercol, K.B. Fielhauer, D.G. Grant, T.J. Hartka, T.A. Hill, S.E. Jaskulek, M.A. Mirantes, L.E. Mosher, M.V. Paul, D.F. Persons, E.H. Rodberg, D.K. Srinivasan, R.M. Vaughan, S.R. Wiley, The MESSENGER spacecraft. Space Sci. Rev. **131**, 187–217 (2007)

J.S. Lewis, Metal/silicate fractionation in the Solar System. Earth Planet. Sci. Lett. **15**, 286–290 (1972)

J.S. Lewis, Chemistry of the planets. Annu. Rev. Phys. Chem. **24**, 339–351 (1974)

L.M. Logan, G.R. Hunt, Emission spectra of particulate silicates under simulated lunar conditions. J. Geophys. Res. **75**, 6539–6548 (1970). https://doi.org/10.1029/JB075i032p06539

L.M. Logan, G.R. Hunt, J.W. Salisbury et al., Compositional implications of Christiansen frequency maximums for infrared remote sensing applications. J. Geophys. Res. **78**, 4983–5003 (1973). https://doi.org/10.1029/JB078i023p04983

P.G. Lucey, B.T. Greenhagen, E. Song, J.A. Arnold, M. Lemelin, K. Donaldson Hanna, N.E. Bowles, T.D. Glotch, D.A. Paige, Space weathering effects in Diviner Lunar Radiometer multispectral infrared measurements of the lunar Christiansen Feature: characteristics and mitigation. Icarus **283**, 343–351 (2017)

P.G. Lucey, D.A. Paige, B.T. Greenhagen, J.L. Bandfield, T.D. Glotch, Comparison of Diviner Christiansen Feature position and visible albedo: Composition and space weathering implications. Lunar Planet. Sci. **41**, 1600 (2010)

D.J.P. Martin, J.F. Pernet-Fisher, K.H. Joy, R.A. Wogelius, A. Morlok, H. Hiesinger, Investigating the shock histories of the lunar meteorites Miller Range 090034, 090070, and 090075 using petrography, geochemistry, and micro-FTIR spectroscopy. Meteorit. Planet. Sci. **52**(6), 1103–1124 (2017). https://doi.org/10.1111/maps.12860

A. Maturilli, J. Helbert, Characterization, testing, calibration, and validation of the Berlin emissivity database. J. Appl. Remote Sens. (2014). https://doi.org/10.1117/1.JRS.8.084985

A. Maturilli, J. Helbert, A. Witzke, L. Moroz, Emissivity measurements of analogue materials for the interpretation of data from PFS on Mars Express and MERTIS on BepiColombo. Planet. Space Sci. **54**, 1057–1064 (2006)

A. Maturilli, J. Helbert, L. Moroz, The Berlin Emissivity Database (BED). Planet. Space Sci. **56**, 420–425 (2008)

A. Maturilli, J. Helbert, J.M. St. John, J.W. Head III., W.M. Vaughan, M. D'Amore, M. Gottschalk, S. Ferrari, Komatiites as Mercury surface analogues: spectral measurements at PEL. Earth Planet. Sci. Lett. **398**, 58–65 (2014). https://doi.org/10.1016/j.epsl.2014.04.035

A. Maturilli, J. Helbert, S. Ferrari, B. Davidsson, M. D'Amore, Characterization of asteroid analogues by means of emission and reflectance spectroscopy in the 1- to 100-µm spectral range. Earth Planets Space **68**, 1–11 (2016a)

A. Maturilli, J. Helbert, S. Ferrari, M. D'Amore, On the effect of emergence angle on emissivity spectra: application to small bodies. Earth Planets Space **68**, 1–9 (2016b)

A. Maturilli, J. Helbert, I. Varatharajan, H. Hiesinger, Emissivity spectra of analogue materials at Mercury P-T conditions. Lunar Planet. Sci. **48**, 1427 (2017)

A. Maturilli, J. Helbert, M. D'Amore, I. Varatharajan, H. Hiesinger, K. Bauch, *The Operations Plan for the MErcury Radiometer and Thermal Infrared Imaging Spectrometer (MERTIS) on Its Way to Mercury* (SPIE, Bellingham, 2018). https://doi.org/10.1117/12.2319940

A. Maturilli, J. Helbert, I. Varatharajan, Graphite as potential darkening agent for Mercury: spectral measurements under simulated Mercury conditions. Lunar Planet. Sci. **50**, 1841 (2019)

T.B. McCord, J.B. Adams, Mercury: surface composition from the reflection spectrum. Science **178**, 745–746 (1972)

T.B. McCord, R.N. Clark, The Mercury soil - presence of $Fe^{2+}$. J. Geophys. Res. **84**, 7664–7668 (1979)

T.J. McCoy, T.L. Dickinson, G.E. Lofgren, Partial melting of the indarch (EH4) meteorite: a textural, chemical and phase relations view of melting and melt migration. Meteorit. Planet. Sci. **34**, 735–746 (1999)

T.J. McCoy, P.N. Peplowksi, F.M. McCubbin, S.Z. Weider, in *Mercury - The View After MESSENGER*, ed. by S.C. Solomon, L.R. Nittler, B.J. Anderson (Cambridge University Press, Cambridge, 2018), pp. 176–190

S.M. Milkovich, J.W. Head, L. Wilson, Identification of mercurian volcanism: resolution effects and implications for MESSENGER. Meteorit. Planet. Sci. **37**, 1209–1222 (2002)

J.W. Morgan, E. Anders, Chemical composition of Earth, Venus, and Mercury. Proc. Natl. Acad. Sci. **77**, 6973–6977 (1980)

A. Morlok, A. Stojic, I. Weber, H. Hiesinger, M. Zanetti, J. Helbert, Mid-infrared bi-directional reflectance spectroscopy of impact melt glasses and tektites. Icarus **278**, 162–179 (2016a). https://doi.org/10.1016/j.icarus.2016.06.013

A. Morlok, A. Stojic, I. Dittmar, H. Hiesinger, M. Tiedeken, M. Sohn, I. Weber, J. Helbert, Mid-infrared spectroscopy of impactites from the Nördlinger Ries impact crater. Icarus **264**, 352–368 (2016b)

A. Morlok, A. Bischoff, M. Patzek, M. Sohn, H. Hiesinger, Chelyabinsk – a rock with many different (stony) faces: an infrared study. Icarus **284**, 431–442 (2017a). https://doi.org/10.1016/j.icarus.2016.11.030

A. Morlok, S. Klemme, I. Weber, A. Stojic, H. Hiesinger, M. Sohn, IR spectroscopy of synthetic glasses with Mercury surface compositions: analogs for remote sensing. Icarus **296**, 123–138 (2017b). https://doi.org/10.1016/j.icarus.2017.05.024

A. Morlok, S. Klemme, I. Weber, A. Stojic, M. Sohn, H. Hiesinger, FTIR reflectance and raman studies of synthetic glass with planetary compositions. Lunar Planet. Sci. **48**, 1824 (2017c)

A. Morlok, S. Klemme, I. Weber, A. Stojic, M. Sohn, H. Hiesinger, J. Helbert, Mid-infrared spectroscopy of planetary analogs: a database for planetary remote sensing. Icarus **324**, 86–103 (2019). https://doi.org/10.1016/j.icarus.2019.02.010

A. Morlok, C. Hamann, D. Martin, I. Weber, K.H. Joy, H. Hiesinger, R. Wogelius, A.N. Stojic, H. Helbert, Mid-infrared spectroscopy of laser-produced basalt melts for remote sensing application. Icarus **335**, 113410 (2020a). https://doi.org/10.1016/j.icarus.2019.113410

A. Morlok, I. Weber, A.N. Stojic, M. Sohn, A. Bischoff, D. Martin, H. Hiesinger, J. Helbert, Mid-infrared reflectance spectroscopy of aubrite components. Meteorit. Planet. Sci. (2020b). https://doi.org/10.1111/maps.13568

A. Morlok, B. Schiller, I. Weber, M. Melwani Daswani, A.N. Stojic, M.P. Reitze, T. Gramse, S.D. Wolters, H. Hiesinger, M.M. Grady, J. Helbert, Mid-infrared reflectance spectroscopy of carbonaceous chondrites and calcium-aluminum-rich inclusions. Planet. Space Sci. (2020c). https://doi.org/10.1016/j.pss.2020.105078, in press

V.I. Moroz, Infrared spectrum of Mercury ($\lambda = 1.0$–$3.9\mu$). Sov. Astron. **8**, 882–889 (1965)

D. Morrison, Thermophysics of the planet Mercury. Space Sci. Rev. **11**, 271–307 (1970). https://doi.org/10.1007/BF00241524

B.C. Murray, Mercury. Sci. Am. **233**, 58–68 (1975)

B.C. Murray, R.G. Strom, N.J. Trask, D.E. Gault, Surface history of Mercury - implications for terrestrial planets. J. Geophys. Res. **80**, 2508–2514 (1975)

J.F. Mustard, J.E. Hays, Effects of hyperfine particles on reflectance spectra from 0.3 to 25 µm. Icarus **125**, 145–163 (1997)

M. Nakamura, T. Imamura, M. Ueno, N. Iwagami, T. Satoh, S. Watanabe, M. Taguchi, Y. Takahashi, M. Suzuki, T. Abe, L. Hashimoto, T. Sakanoi, S. Okano, Y. Kasaba, J. Yoshida, M. Yamada, N. Ishii, T. Yamada, K. Uemizu, T. Fukuhara, K. Oyama, Planet-C: Venus Climate Orbiter mission of Japan. Planet. Space Sci. **55**, 1831–1842 (2007)

O. Namur, B. Charlier, Silicate mineralogy at the surface of Mercury. Nat. Geosci. **10**, 9–13 (2017)

D.B. Nash, J.W. Salisbury, Infrared reflectance spectra (2.2-15 µm) of plagioclase feldspars. Geophys. Res. Lett. **18**, 1151–1154 (1991). https://doi.org/10.1029/91GL01008

D.B. Nash, J.W. Salisbury, J.E. Conel, P.G. Lucey, P.R. Christensen, Evaluation of infrared emission spectroscopy for mapping the Moon's surface composition from lunar orbit. J. Geophys. Res. **98**, 23535–23552 (1993). https://doi.org/10.1029/93JE02604

L.R. Nittler, R.D. Starr, S.Z. Wieder, T.J. McCoy, W.V. Boynton, D.S. Ebel, C.M. Ernst, L.G. Evans, J.O. Goldsten, D.K. Hamara, D.J. Lawrence, R.L McNutt Jr., C.E. Schlemm, S.C. Solomon, A.L. Sprague, The major-element composition of Mercury's surface from MESSENGER X-ray spectrometry. Science **333**, 1847–1850 (2011)

L.R. Nittler, N.L. Chabot, T.L. Grove, P.N. Peplowski, The chemical composition of Mercury, in *Mercury II*, ed. by J.C. Solomon, L.R. Nittler, B.J. Anderson (University of Arizona Press, Tucson, 2018), pp. 30–51

S.K. Noble, C.M. Pieters, Space weathering on Mercury: implications for remote sensing. Sol. Syst. Res. **37**, 31–35 (2003)

S.K. Noble, C.M. Pieters, L.A. Taylor, R.V. Morris, C.C. Allen, D.S. McKay, L.P. Keller, The optical properties of the finest fraction of lunar soil: implications for space weathering. Meteorit. Planet. Sci. **36**, 31–42 (2001)

D. Oertel, D. Spänkuch, H. Jahn, H. Becker-Ross, W. Stadthaus, J. Nopirakowski, W. Döhler, K. Schäfer, J. Güldner, R. Dubois, V.I. Moroz, V.M. Linkin, V.V. Kerzhanovich, I.A. Matsgorin, A.N. Lipatov, A.A. Shurupov, L.V. Zasova, E.A. Ustinov, Infrared spectrometry of Venus from "Venera-15" and "Venera-16". Adv. Space Res. **5**, 25–36 (1985)

D.A. Paige, M.C. Foote, B.T. Greenhagen, J.T. Schofield, S. Calcutt, A.R. Vasavada, D.J. Preston, F.W. Taylor, C.C. Allen, K.J. Snook, B.M. Jakosky, B.C. Murray, L.A. Soderblom, B. Jau, S. Loring, J. Bulharowski, N.E. Bowles, I.R. Thomas, M.T. Sullivan, C. Avis, E.M. De Jong, W. Hartford, D.J. McCleese, The lunar reconnaissance orbiter diviner lunar radiometer experiment. Space Sci. Rev. **150**, 125–160 (2010)

P.N. Peplowski, R.L. Klima, D.J. Lawrence, C.M. Ernst, B.W. Denevi, E.A. Frank, J.O. Goldsten, S.L. Murchie, L.R. Nittler, S.C. Solomon, Remote sensing evidence for an ancient carbon-bearing crust on Mercury. Nat. Geosci. **9**, 273–276 (2016)

G. Peter, J. Helbert, H. Hiesinger, I. Weber, I. Walter, G. Arnold, T. Säuberlich, G. Páez, Developing of MERTIS as an advanced process from the study up to the flight model, in *SPIE Infrared Rem. Sens. Instr.*, vol. 8867, p. 886707 (2013). https://doi.org/10.1117/12.2024375

C.M. Pieters, E.M. Fischer, O. Rode, A. Basu, Optical effects of space weathering: the role of the finest fraction. J. Geophys. Res. **98**, 20,817–20,824 (1993)

C.M. Pieters, L.A. Taylor, S.K. Noble, L.P. Keller, B. Hapke, R.V. Morris, C.C. Allen, D.S. McKay, S. Wentworth, Space weathering on airless bodies: resolving a mystery with lunar samples. Meteorit. Planet. Sci. **35**, 1101–1107 (2000)

A. Pisello, M.C. De Sanctis, A. Maturilli, S. De Angelis, M. Ferrari, F. Vetere, C. Pauselli, D. Perugini, Spectroscopy on silicate glasses from two magmatic series: implications for planetary studies, in *EPSC Abstracts*, vol. 12 (2018), EPSC2018-901

F. Poulet, S. Erard, Nonlinear spectral mixing: quantitative analysis of laboratory mineral mixtures. J. Geophys. Res. **109** (2004). https://doi.org/10.1029/2003JE002179

B. Rava, B. Hapke, An analysis of the Mariner 10 color ratio map of Mercury. Icarus **71**, 397–429 (1987)

M.P. Reitze, I. Weber, H. Kroll, A. Morlok, H. Hiesinger, J. Helbert, Mid-infrared spectroscopy of alkali feldspar samples for space application. Mineral. Petrol. (2020). https://doi.org/10.1007/s00710-020-00709-9

M. Robinson, P. Lucey, Recalibrated Mariner 10 color mosaics: implications for mercurian volcanism. Science **275**, 197–200 (1997)

M.S. Robinson, G.I. Taylor, Ferrous oxide in Mercury's crust and Mantle. Meteorit. Planet. Sci. **36**, 841–847 (2001)

M.S. Robinson, C.R. Chapman, D.L. Domingue, S.E. Hawkins, J.W. Head, G.M. Holsclaw, W.E. McClintock, R.L. McNutt, S.L. Murchie, L.M. Prockter, R.G. Strom, T.C. Watters, D.T. Bewett, J.J. Gillis-Davis, S.C. Solomon, Mercury color and albedo: new insights from MESSENGER. Lunar Planet. Sci. **39**, 1187 (2008)

D. Rommel, A. Grumpe, M.P. Felder, C. Wöhler, U. Mal, A. Kronz, Automatic endmember selection and nonlinear spectral unmixing of lunar analog minerals. Icarus **284**, 126–149 (2017). https://doi.org/10.1016/j.icarus.2016.10.029

D. Rothery, L. Mariangeli, K. Joy, P. Potts, U. Christensen, J. Carpenter, J. Näränen, K. Muinonen, M. Anad, C. Pauselli, A. Frigeri, G. Fraser, S. Erard, E. Hauber, A. Milillo, P. Wurz, M.C. De Sanctis, M. Massironi, E.M. Epifani, J. Helbert, H. Hiesinger, I. Mitrofanov, Mercury's surface and composition to be studied by BepiColombo. Planet. Space Sci. **58**, 21–39 (2010). https://doi.org/10.1016/j.pss.2008.09.001

D.A. Rothery, M. Massironi, G. Alemanno, B. Barraud, S. Besse, N. Bott, R. Brunetto, E. Bunce, P. Byrne, M.T. Capria, F. Capaccioni, C. Carli, B. Charlier, T. Cornet, G. Cremonese, M. D'Amore, M.C. De Sanctis, A. Doressoundiram, L. Ferranti, G. Filacchione, V. Galluzzi, L. Giacomini, M. Grande, L.G. Guzzetta, J. Helbert, D. Heyner, H. Hiesinger, R. Hyodo, T. Kohout, A. Lucchetti, C. Malliband, P. Mancinelli, J. Martikainen, A. Martindale, A. Maturilli, A. Milillo, A. Morlok, K. Muinonen, O. Namur, L.R. Nittler, J.S. Oliveira, P. Palumbo, M. Pajola, D. Pegg, A. Penttilä, R. Politi, C. Re, C. Stangarone, A. Stojic, T. Väisänen, I. Varatharajan, I. Weber, J. Wright, P. Wurz, F. Zambon, Rationale for BepiColombo studies of Mercury's surface and composition. Space Sci. Rev. **216**, 66 (2020). https://doi.org/10.1007/s11214-020-00694-7

J.W. Salisbury, Mid-infrared spectroscopy: laboratory data, in *Topics in Remote Sensing*, vol. 4, ed. by C.M. Pieters, P.A.J. Englert (1993), pp. 79–98, Cambridge

J.W. Salisbury, A. Basu, E.M. Fischer, Thermal infrared spectra of lunar soils. Icarus **130**, 125–139 (1997)

J.W. Salisbury, A. Wald, The role of volume scattering in reducing spectral contrast of Reststrahlen bands in spectra of powdered minerals. Icarus **96**, 121–128 (1992)

G. Schubert, T. Spohn, Thermal history of Mars and the sulfur content of its core. J. Geophys. Res. **95**, 14095–14104 (1990)

K.A. Shirley, T.D. Glotch, Particle size effects on mid-infrared spectra of lunar analog minerals in a simulated lunar environment. J. Geophys. Res. **124** (2019). https://doi.org/10.1029/2018JE005533

K.A. Shirley, D. McDougall, T.D. Glotch, The effect of albedo on mid-infrared spectra of airless bodies with implications for Diviner data analysis. Lunar Planet. Sci. **49**, 1298 (2018)

M.A. Slade, B.J. Butler, D.O. Muhleman, Mercury radar imaging - evidence for polar ice. Science **258**, 635–640 (1992)

S.C. Solomon, Mercury: the enigmatic innermost planet. Earth Planet. Sci. Lett. **216**, 441–455 (2003)

S.C. Solomon, R.L. McNutt Jr., R.E. Gold, M.H. Acuña, D.N. Baker, W.V. Boynton, C.R. Chapman, A.F. Cheng, G. Gloeckler, J.W. Head III., S.M. Krimigis, W.E. McClintock, S.L. Murchie, S.J. Peale, R.J. Phillips, M.S. Robinson, J.A. Slavin, D.E. Smith, R.G. Strom, J.I. Trombka, M.T. Zuber, The MESSENGER mission to Mercury: scientific objectives and implementation. Planet. Space Sci. **49**, 1445–1465 (2001)

T. Spohn, F. Sohl, K. Wieczerkowski, V. Conzelmann, The interior structure of Mercury: what we know, what we expect from BepiColombo. Planet. Space Sci. **49**, 1561–1570 (2001)

A.L. Sprague, T.L. Roush, Comparison of laboratory emission spectra with Mercury telescopic data. Icarus **133**, 174–183 (1998)

A.L. Sprague, R.W.H. Kozlowski, F.C. Witteborn, D.P. Cruikshank, D.H. Wooden, Mercury: evidence for anorthosite and basalt from mid-infrared (7.3–13.5 micrometers) spectroscopy. Icarus **109**, 156–167 (1994)

A.L. Sprague, D.M. Hunten, K. Lodders, Sulfur at Mercury, elemental at the poles and sulfides in the regolith. Icarus **118**, 211–215 (1995). Erratum: Icarus **123**, 247

A.L. Sprague, D.B. Nash, F.C. Witteborn, D.P. Cruikshank, Mercury's feldspar connection - mid-IR measurements suggest plagioclase. Adv. Space Res. **19**, 1507–1510 (1997)

A.L. Sprague, J.P. Emery, K.L. Donaldson, R.W. Russell, D.K. Lynch, A.L. Mazuk, Mercury: mid-infrared (3-13.5 µm) observations show heterogeneous composition, presence of intermediate and basic soil types, and pyroxene. Meteorit. Planet. Sci. **37**, 1255–1268 (2002)

A.L. Sprague, K.L. Donaldson Hanna, RW. Kozlowski, J. Helbert, A. Maturilli, J.B. Warell, J.L. Hora, Spectral emissivity measurements of Mercury's surface indicate Mg- and Ca-rich mineralogy, K-spar, Na-rich plagioclase, rutile, with possible perovskite, and garnet. Planet. Space Sci. **57**, 364–383 (2009). https://doi.org/10.1016/j.pss.2009.01.006

P.D. Spudis, J.E. Guest, Stratigraphy and geologic history of Mercury, in *Mercury*, ed. by F. Vilas, C.R. Chapman, M.S. Matthews (University of Arizona Press, Tucson, 1988), pp. 118–164

L.J. Srnka, Magnetic dipole moment of a spherical shell with TRM acquired in a field of internal origin. Phys. Earth Planet. Inter. **11**, 184–190 (1976)

C. Stangarone, J. Helbert, A. Maturilli, M. Tribaudino, M. Prencipe, Modelling of thermal-IR spectra of forsterite: application on remote sensing for Mercury, in *EPSC Abstracts*, vol. 11 (2017), EPSC2017-841

L.V. Starukhina, Water detection on atmosphereless celestial bodies: alternative explanations of the observations. J. Geophys. Res. **106**, 14701–14710 (2001)

A. Stephenson, Crustal remanence and the magnetic moment of Mercury. Earth Planet. Sci. Lett. **28**, 454–458 (1976)

A.N. Stojic, A. Morlok, M. Sohn, H. Hiesinger, T. Kohout, H. Aurich, I. Weber, J. Helbert, A shock recovery experiment: tracing spectral fingerprints of impact melt, npFe and element migration in shocked porous materials, in *EPSC Abstracts*, vol. 13 (2019). EPSC-DPS2019-521-1

B.E. Strauss, J.M. Feinberg, C.L. Johnson, Magnetic mineralogy of the Mercurian lithosphere. J. Geophys. Res., Planets **121**, 2225 (2016)

R.G. Strom, Mercury: an overview. Adv. Space Res. **19**, 1471–1485 (1997)

R.G. Strom, A.L. Sprague, *Exploring Mercury: The Iron Planet* (Springer, Chichester, 2003). 216 pp.

R.J. Thomas, D.A. Rothery, S.J. Conway, M. Anand, Long-lived explosive volcanism on Mercury. Geophys. Res. Lett. **41**, 6084–6092 (2014)

J.L. Thompson, J.W. Salisbury, The mid-infrared reflectance of mineral mixtures (7-14 µm). Remote Sens. Environ. **45**, 1–13 (1993)

D. Trang, P.G. Lucey, N.R. Izenberg, Radiative transfer modeling of MESSENGER VIRS spectra: detection and mapping of submicroscopic iron and carbon. Icarus **293**, 206–217 (2017)

N.J. Trask, R.G. Strom, Additional evidence of mercurian volcanism. Icarus **28**, 559–563 (1976)

A.L. Tyler, R.W.H. Kozlowski, L.A. Lebofsky, Determination of rock type on Mercury and the moon through remote sensing in the thermal infrared. Geophys. Res. Lett. **15**, 808–811 (1988)

K.E. Vander Kaaden, F.M. McCubbin, Exotic crust formation on Mercury: consequences of a shallow, FeO-poor mantle. J. Geophys. Res., Planets **120**, 195–209 (2015)

K.E. Vander Kaaden, F.M. McCubbin, L.R. Nittler, P.N. Peplowski, S.Z. Weider, E.A. Frank, T.J. McCoy, Geochemistry, mineralogy, and petrology of boninitic and komatiitic rocks on the mercurian surface: insights into the mercurian mantle. Icarus **285**, 155–168 (2017)

I. Varatharajan, A. Maturilli, J. Helbert, G. Ulrich, K. Born, O. Namur, B. Kästner, L. Hecht, B. Charlier, H. Hiesinger, Nano-FTIR spectroscopy to investigate the silicate mineralogy of Mercury analogues: supporting MERTIS onboard BepiColombo mission. Lunar Planet. Sci. **49**, 6067 (2018a)

I. Varatharajan, A. Maturilli, J. Helbert, G. Ulrich, K. Born, O. Namur, B. Kästner, L. Hecht, B. Charlier, H. Hiesinger, Bi-directional reflectance and NanoFTIR spectroscopy of synthetic analogues of Mercury: supporting MERTIS payload of ESA/JAXA BepiColombo mission, in *EPSC Abstracts*, vol. 12 (2018b), EPSC2018-763-1

I. Varatharajan, A. Maturilli, J. Helbert, G. Alemanno, H. Hiesinger, Spectral behavior of sulfides in simulated daytime surface conditions of Mercury: supporting past (MESSENGER) and future missions (BepiColombo). Earth Planet. Sci. Lett. **520**, 127–140 (2019a)

I. Varatharajan, C. Tsang, K. Wohlfarth, C. Wöhler, N. Izenberg, J. Helbert, Surface composition of Mercury from NIR (0.7-4.2 µm) ground-based IRTF/SpeX spectroscopy, in *EPSC Abstracts*, vol. 13 (2019b). EPSC-DPS2019-1331-2

I. Varatharajan, C. Stangarone, A. Maturilli, J. Helbert, H. Hiesinger, Emissivity of powdered silicates in TIR spectral range (7-14 µm) under simulated daytime surface conditions of Mercury and their detection from the orbit. Lunar Planet. Sci. **51**, 1962 (2020)

W.M. Vaughan, J. Helbert, D.T. Blewett, J.W. Head, S.L. Murchie, K. Gwinner, T.J. McCoy, S.C. Solomon, Hollow-forming layers in impact craters on Mercury: massive sulfide or chloride deposits formed by impact melt differentiation? Lunar Planet. Sci. **43**, 1187 (2012)

F. Vilas, Mercury: absence of crystalline $Fe^{2+}$ in the regolith. Icarus **64**, 133–138 (1985)

F. Vilas, Surface composition of Mercury from reflectance spectrophotometry, in *Mercury*, ed. by F. Vilas, C.R. Chapman, M.S. Matthews (University of Arizona Press, Tucson, 1988), pp. 59–76

F. Vilas, T.B. McCord, Mercury: spectral reflectance measurements (0.33-1.06 µm) 1974/75. Icarus **28**, 593–599 (1976)

F. Vilas, M.A. Leake, W.W. Mendell, The dependence of reflectance spectra of Mercury on surface terrain. Icarus **59**, 60–68 (1984)

J. Warell, Properties of the hermean regolith. II. Disk-resolved multicolor photometry and color variations of the "unknown" hemisphere. Icarus **156**, 303–317 (2002)

J. Warell, Properties of the hermean regolith: III. Disk-resolved vis-NIR reflectance spectra and implications for the abundance of iron. Icarus **161**, 199–222 (2003)

J. Warell, D.T. Blewett, Properties of the hermean regolith: V. New optical reflectance spectra, comparison with lunar anorthosites, and mineralogical modelling. Icarus **168**, 257–276 (2004)

J.A. Warell, A. Sprague, J. Emery, R.W. Kozlowski, A. Long, The 0.7–5.3 micrometer IR spectra of Mercury and the Moon: evidence for high-Ca clinopyroxene on Mercury. Icarus **180**, 281–291 (2006)

J.T. Wasson, The building stones of the planets, in *Mercury*, ed. by F. Vilas, C.R. Chapman, M.S. Matthews (University of Arizona Press, Tucson, 1988), pp. 622–650

I. Weber, A. Morlok, A. Bishoff, D. Ward, H. Hiesinger, K.H. Joy, S.A. Crowther, H. Barden, N.D. Jastrzebski, J.D. Gilmour, R.A. Wogelius, R.C. Greenwood, I.A. Franchi, C. Münker, Cosmochemical and spectroscopic properties of Northwest Africa 7325 – a consortium study. Meteorit. Planet. Sci. **51**, 3–30 (2016). https://doi.org/10.1111/maps.12586

I. Weber, A. Morlok, T. Grund, K.E. Bauch, H. Hiesinger, A.N. Stojic, A. Grumpe, C. Wöhler, S. Klemme, M. Sohn, D.J.P. Martin, K.H. Joy, A mid-infrared reflectance database in preparation for space missions. Lunar Planet. Sci. **49**, 1430 (2018)

I. Weber, A. Morlok, M. Heeger, T. Adolphs, M.P. Reitze, H. Hiesinger, K.E. Bauch, A.N. Stojic, H.F. Arlinghaus, J. Helbert, Simulating space weathering on Mercury: excimer laser experiments on mineral mixtures. Lunar Planet. Sci. **50**, 2326 (2019)

I. Weber, M.P. Reitze, A. Morlok, M. Heeger, T. Adolphs, K.E. Bauch, H. Hiesinger, A.N. Stojic, H.F. Arlinghaus, J. Helbert, Data processing for space missions: MID-FTIR reflectance measurements of mineral mixtures. Lunar Planet. Sci. **51**, 1889 (2020a)

I. Weber, A.N. Stojic, A. Morlok, H. Hiesinger, S.G. Pavlov, K. Markus, R. Wirth, A. Schreiber, M. Sohn, H.-W. Hübers, Laser-irradiated olivine and pyroxene: a coordinated TEM and IR spectroscopic study. Earth Planet. Sci. Lett. **530** (2020b). https://doi.org/10.1016/j.epsl.2019.115884

S.J. Weidenschilling, Iron/silicate fractionation and the origin of Mercury. Icarus **35**, 99–111 (1978)

S.Z. Weider, L.R. Nittler, R.D. Starr, T.J. McCoy, K.R. Stockstill-Cahill, P.K. Byrne, B.W. Denevi, J.W. Head, S.C. Solomon, Chemical heterogeneity on Mercury's surface revealed by the MESSENGER X-Ray Spectrometer. J. Geophys. Res. **117** (2012). https://doi.org/10.1029/2012JE004153

S.Z. Weider, L.R. Nittler, R.D. Starr, T.J. McCoy, S.C. Solomon, Variations in the abundance of iron on Mercury's surface from MESSENGER x-ray spectrometer observations. Icarus **235**, 170–186 (2014)

G.W. Wetherill, Accumulation of Mercury from planetesimals, in *Mercury*, ed. by F. Vilas, C.R. Chapman, M.S. Matthews (University of Arizona Press, Tucson, 1988), pp. 670–691

R.A. Wiesli, B.L. Beard, L.A. Taylor, C.M. Johnson, Space weathering processes on airless bodies: Fe isotope fractionation in the lunar regolith. Earth Planet. Sci. Lett. **216**, 457–465 (2003). https://doi.org/10.1016/S0012-821X(03)00552-1